Monthly Notices of the ROYAL ASTRONOMICAL SOCIETY

MNRAS **501,** 4396–4419 (2021) doi:10.1093/mnras/staa3870
Advance Access publication 2020 December 18

The distribution and properties of DLAs at $z \leq 2$ in the EAGLE simulations

Lilian Garratt-Smithson [1,2]★ Chris Power [1,2] Claudia del P. Lagos,[1,2,3] Adam R. H. Stevens [1,2] James R. Allison [2,4] and Elaine M. Sadler [2,5,6]

[1]*International Centre for Radio Astronomy Research, University of Western Australia, 35 Stirling Highway, Crawley, WA 6009, Australia*
[2]*ARC Centre of Excellence for All-sky Astrophysics in 3 Dimensions (ASTRO 3D), Australia*
[3]*Cosmic Dawn Center (DAWN), Niels Bohr Institute, University of Copenhagen, Nørregade, Copenhagen DK-0000-0003-3631-7176, Denmark*
[4]*Sub-Department of Astrophysics, Department of Physics, University of Oxford, Denys Wilkinson Building, Keble Rd., Oxford OX1 3RH, UK*
[5]*Sydney Institute for Astronomy, School of Physics A28, University of Sydney, Sydney, NSW 2006, Australia*
[6]*CSIRO Astronomy and Space Science, PO Box 76, Epping, NSW 1710, Australia*

Accepted 2020 December 13. Received 2020 December 9; in original form 2020 August 17

ABSTRACT

Determining the spatial distribution and intrinsic physical properties of neutral hydrogen on cosmological scales is one of the key goals of next-generation radio surveys. We use the EAGLE galaxy formation simulations to assess the properties of damped Lyman α absorbers (DLAs) that are associated with galaxies and their underlying dark matter haloes between $0 \leq z \leq 2$. We find that the covering fraction of DLAs increases at higher redshift; a significant fraction of neutral atomic hydrogen (H I) resides in the outskirts of galaxies with stellar mass $\geq 10^{10}$ M$_\odot$; and the covering fraction of DLAs in the circumgalactic medium (CGM) is enhanced relative to that of the interstellar medium (ISM) with increasing halo mass. Moreover, we find that the mean density of the H I in galaxies increases with increasing stellar mass, while the DLAs in high- and low-halo mass systems have higher column densities than those in galaxies with intermediate halo masses ($\sim 10^{12}$ M$_\odot$ at $z = 0$). These high-impact CGM DLAs in high-stellar mass systems tend to be metal poor, likely tracing smooth accretion. Overall, our results point to the CGM playing an important role in DLA studies at high redshift ($z \geq 1$). However, their properties are impacted both by numerical resolution and the detailed feedback prescriptions employed in cosmological simulations, particularly that of active galactic nuclei.

Key words: galaxies: evolution – galaxies: ISM – quasars: absorption lines.

1 INTRODUCTION

Hydrogen is the most abundant element in the Universe and H I (atomic hydrogen) has been linked with fundamental galaxy properties such as star formation rate (SFR) and star formation efficiency (SFE), stellar mass, morphology, metallicity, and colour (e.g. Zhang et al. 2009; Cortese et al. 2011; Wang et al. 2011; Hughes et al. 2013; Saintonge et al. 2016; Wang et al. 2017; Zhou et al. 2018). Additionally, the column density of H I is also known to increase towards the centre of galaxies (e.g. Rahmati & Schaye 2014; Prochaska et al. 2017; Rhodin et al. 2018). These correlations imply an intrinsic link between H I and internal galactic processes.

There existed at least twice as much H I in the high-redshift Universe ($z \sim 2$) than today (e.g. Prochaska & Wolfe 2009; Neeleman et al. 2016; Sánchez-Ramírez et al. 2016; Bird, Garnett & Ho 2017; Rhee et al. 2018). However, the evolution of the cosmic H I mass density ($\Omega_{\rm H\,I}$) is relatively weak compared with the evolution of $\Omega_{\rm H_2}$ (the cosmic molecular hydrogen mass density), which declines by a factor of 3–10 from $z \sim 2$ to 0 (Decarli et al. 2019), along with $\Omega_{\rm SFR}$ (the cosmic SFR density), which shows a sharp peak at $z \sim 2$ (Madau & Dickinson 2014; Driver et al. 2018) and drops by an order of magnitude ($\sim 20\times$) to the present-day Universe. This suggests H I is replenished throughout cosmic time but that the conversion efficiency into H_2 and SFR is evolving. Recent studies have indicated that the H I reservoir inside a galaxy to be highly dynamic and existing in a state of flux, accreting on to a galaxy initially as ionized inflows and fuelling further star formation on Gyr time-scales (e.g. Davé et al. 2013; Crain et al. 2017). Chowdhury et al. (2020) recently used H I 21-cm emission stacking to obtain an $\Omega_{\rm H\,I}$ value that is consistent with previous optical measurements using Mg II absorbers and UV DLAs, while also finding the average $M_{\rm H\,I}$-to-SFR ratio suggests a relatively short H I depletion time-scale (of the order of a few Gyr).

H I ubiquitously emits and absorbs at a wavelength of 21 cm. 21-cm absorption line studies are an important tool for studying H I in the early Universe, particularly since the sensitivity of absorption line surveys is independent of redshift. This is in contrast to H I emission, which is very weak for distant galaxies (e.g. Fernández et al. 2016). Practically, to observe 21-cm absorption requires a background source that is bright in the radio. This is normally a quasar.

The next generation of blind 21-cm absorption surveys will open up a new area of parameter space (for a recent example, see work by Grasha et al. 2020, who use H I 21-cm absorption in the redshift range $0 < z \leq 2.74$ to place constraints on the cosmic evolution of $\Omega_{\rm H\,I}$). In particular, both the MeerKAT Absorption Line Survey (MALS; Gupta et al. 2016) and the First Large Absorption Survey in H I (FLASH; Allison et al. 2020) are two dedicated 21-cm absorption surveys at cosmological distances. Here, we focus on FLASH, which

★ E-mail: lilian.garratt-smithson@uwa.edu.au

© 2020 The Author(s)
Published by Oxford University Press on behalf of Royal Astronomical Society

Downloaded from https://academic.oup.com/mnras/article/501/3/4396/6041704 by Bodleian Library of the University of Oxford user on 01 April 2021

is a blind 21-cm survey of the entire southern sky, probing 150 000 sightlines in the redshift range 0–1 with the Australian Square Kilometre Array Pathfinder (ASKAP; Johnston et al. 2007).

FLASH will be sensitive to the highest column density H I gas (see fig. 6 of Allison et al. 2016) and hence most likely DLAs (damped Lyman α systems, defined as systems with $N_{\rm H\,I}$ values of greater than 2×10^{20} cm^{-2}; for a review see Wolfe, Gawiser & Prochaska 2005). DLAs are thought to typically arise in the inner 30 kpc of a galaxy, since column density appears to anticorrelate with impact parameter (e.g. Rahmati & Schaye 2014; Rubin et al. 2015). In this way, DLAs are expected to trace the crucial star formation processes inside a galaxy, in particular the cooling of atomic to molecular hydrogen, which is the fuel for further star formation. Additionally, 21-cm absorption is sensitive to the harmonic mean 21-cm excitation temperature, which in turn is dependent on the fraction of the CNM (cold neutral medium; e.g. Kanekar et al. 2014; Allison et al. 2016). Therefore, 21-cm surveys are sensitive to the coldest gas in the galaxy, unlike optical DLA searches that trace the total H I content.

Recently, Allison et al. (2020) demonstrated early science results from FLASH by carrying out a blind survey for 21-cm absorption in the GAMA 23 field (Liske et al. 2015). They detected absorption in the outskirts (impact parameter = 17 kpc) of an intervening early-type galaxy, showing that substantial column densities of cold absorbing gas can be found at large distances (presumably in an H I disc) in such galaxies. Additionally, in ASKAP commissioning observations of a sample of radio-loud quasars, Sadler et al. (2020) obtained a measurement of the incidence of DLAs at $0.4 < z < 1$ that was consistent with previous measurements within the current uncertainties. These measurements will improve by two orders of magnitude once FLASH is complete

Due to observational limits (i.e. the use of optical telescopes) DLAs have been well studied at $z > 2$, the range where the rest-frame UV Lyman α line is redshifted into the optical. Surveys such as the Sloan Digital Sky Survey (SDSS; York et al. 2000; Noterdaeme et al. 2009, 2012) have been critical to provide a range of valuable observations. However, at $z < 1$, it has been particularly difficult to obtain a sample of unbiased DLAs. The common approach has been to use SDSS to pre-select Mg II absorbers (e.g. Turnshek et al. 2005) and then follow these up with space UV spectrographs, such as the *Hubble Space Telescope* (for a recent example see Monier et al. 2019). It is, however, unclear whether this approach delivers a representative sample of intermediate-redshift DLAs, with some tension in the derived $\Omega_{\rm H\,I}$ seen in the literature (e.g. Neeleman et al. 2016; Berg et al. 2017; Rao et al. 2017). FLASH will observe DLAs in the radio towards radio-bright galaxies, and hence will provide the first unbiased view of neutral hydrogen in the Universe at intermediate redshifts.

From observational studies, we still have a limited understanding of DLA host galaxies, primarily due to the lack of follow-up detections in multiwavelength emission (e.g. Fynbo et al. 2011; Péroux et al. 2011; Fumagalli et al. 2015; Rahmani et al. 2016). The lack of follow-up detections is attributed both to contamination from the background light of the quasar (e.g. Møller & Warren 1998), along with the fact DLAs are thought to trace galaxies with a wide range of galaxy properties, which makes them a more representative sample of the overall galaxy population (e.g. Krogager et al. 2017). It also means a large number of DLAs are likely to be associated with faint, low-mass galaxies that are below the emission detection limit (e.g. Fumagalli et al. 2015). There have been a number of observational papers that look at the properties of DLAs, in particular their metallicities (e.g. Rafelski et al. 2014; Krogager et al. 2017) and kinematics (e.g. Prochaska & Wolfe 1997), but their physical nature is still debated.

Hydrodynamical simulations, alongside semi-analytical models of galaxy formation, offer a way to theoretically investigate the physical origin of DLAs and their host galaxy properties, free from observational selection effects (examples of simulations/models investigating DLAs include Altay et al. 2013; Berry et al. 2014; Rahmati et al. 2015; Berry et al. 2016; Rhodin et al. 2019; van de Voort et al. 2019). There has been a large number of previous works investigating the number density of DLAs in cosmological hydrodynamical simulations and how this varies with properties of the host galaxy such as stellar mass and star formation rate, along with the range of impact parameters possible (e.g. Bird et al. 2014; Rahmati & Schaye 2014). Similar to the observations, this work has typically been focused at $z \geq 2$, and simulations/models suggest DLAs trace a representative sample of galaxies. Moreover, the majority are considered to be hosted by faint low-halo-mass systems and thus have low-star formation rates (e.g. Bird et al. 2014; Rahmati & Schaye 2014). Work using theoretical models has also suggested that the physical origin of DLAs is redshift dependent, where DLAs of $z > 3$ are likely to arise from intergalactic gas filaments, while those below this redshift are likely to originate from the galactic disc (Berry et al. 2014).

Due to the high computational demand of resolving the cold neutral interstellar medium (ISM) of galaxies, a number of recent theoretical studies have used cosmological zoom simulations (e.g. Rhodin et al. 2019), which can resolve cooling below 10^4 K and hence model H I self-consistently throughout the simulation. In particular, simulations such as these have shed light on the contribution of the CGM (circumgalactic medium)/gaseous halo to the DLA population. However, these smaller scale simulations lose the large number statistics required to compare with surveys.

In order to interpret the results from FLASH, it is important to make predictions about (a) the distribution of H I in and around galaxies at this redshift range as a function of their properties (e.g. halo mass, stellar kinematics) and (b) the properties of DLAs associated with galaxies in this redshift range. In this paper, we hope to address both questions by utilizing the Evolution and Assembly of GaLaxies and their Environments (EAGLE) cosmological simulations (Schaye et al. 2015).

Previous work has shown EAGLE boxes of varying resolution are able to largely reproduce a wide range of cold gas properties (despite not been calibrated to do so), including the observed clustering of H I systems (Crain et al. 2017), the global H I column density distribution function (Rahmati et al. 2015), the observed H I morphologies of galaxies and in particular their radial profiles (Bahé et al. 2016), along with their H_2 properties (Lagos et al. 2015, 2016). For a recent detailed analysis of the cold gas contents in EAGLE and other cosmological simulations (see Davé et al. 2020).

In this paper, we are particularly interested in investigating further the distribution of strong DLAs in galaxies with a wide range of halo masses in the redshift range of interest for FLASH. We are also interested in the relative contribution of the CGM and how this varies with galaxy properties. Moreover, we will discuss the DLA properties (such as metallicity and impact parameter) and how these vary with host galaxy properties and redshift.

The structure of the paper will be as follows; the next section will explain our numerical methodology, in particular detailing how we obtain the H I mass fractions from EAGLE, along with our method of separating gas particles into the ISM/CGM (Section 2). Our results will follow in Section 3, beginning with the DLA covering fractions

Downloaded from https://academic.oup.com/mnras/article/501/3/4396/6041704 by Bodleian Library of the University of Oxford user on 01 April 2021

in EAGLE galaxies and moving on to the detailed DLA properties. Finally, we give a discussion and our conclusions in Section 4.

2 NUMERICAL METHOD

2.1 The EAGLE simulations

In this paper, we use the public data release of the EAGLE simulation suite (Crain et al. 2015; Schaye et al. 2015; McAlpine et al. 2016; The EAGLE team 2017). EAGLE is a set of cosmological hydrodynamical simulations run using a modified version of the *N*-body/Smoothed Particle Hydrodynamics (SPH) code GADGET-3 (Springel 2005). The modifications to the SPH method are collectively known as 'Anarchy' and include an artificial viscosity switch (Cullen & Dehnen 2010), an artificial thermal conduction switch (Price 2008), a time-step limiter (Durier & Dalla Vecchia 2012), and the pressure–entropy formulation of Hopkins (2013).

Each simulation also includes a wide range of sub-grid physics, including tracking stellar winds from asymptotic giant branch (AGB) stars and supernovae (core-collapse and Type 1a, Wiersma et al. 2009b), along with a stochastic star formation recipe (Schaye & Dalla Vecchia 2008) that also includes a metal-dependant star formation threshold based on Schaye (2004) and is designed to take into account the atomic-molecular transition. Moreover, radiative cooling and heating are included (Wiersma, Schaye & Smith 2009a), along with stellar feedback via a stochastic thermal heating (see Dalla Vecchia & Schaye 2012, for details) and an active galactic nuclei (AGN) feedback scheme based on a modified Bondi–Hoyle accretion rate (Rosas-Guevara et al. 2015) and using the energy threshold described in Schaye et al. (2015). The subgrid parameters were calibrated to reproduce the $z = 0$ galaxy stellar mass function (GSMF), along with the galaxy stellar mass–size relation and the black hole–stellar mass relations. However, the gaseous properties of the galaxies were not calibrated and hence relations that include the gas properties of galaxies can be considered as predictions.

For the majority of results in this paper, we use simulations run at two different volumes; $(100\ \mathrm{cMpc})^3$ (Ref-L0100N1504, referred to as RefL0100 in this paper) and $(25\ \mathrm{cMpc})^3$ (Recal-L0025N0752, referred to as RecalL0025). Our choice was motivated by the intrinsic link between the cold gas fractions of galaxies and the detailed numerical modelling of physical processes such as stellar feedback, which are implemented differently in the two boxes (see below for details). We also use both boxes in order to quantify the effects of numerical resolution on our results. The smaller EAGLE box also allows us to include a greater number of lower stellar-mass galaxies ($<10^{10}$ $\mathrm{M}_\odot$), given these are adequately resolved in the RecalL0025 box. This is advantageous since previous studies (e.g. Bird et al. 2014; Rahmati & Schaye 2014) predict the majority of DLAs to be in low-mass haloes ($M_{200} < 10^{10}$ $\mathrm{M}_\odot$), while there is also evidence for strong DLAs in galaxies of halo mass 10^{11}–10^{12} $\mathrm{M}_\odot$ at $z > 3$ (Mackenzie et al. 2019). Furthermore, Crain et al. (2017) found the standard-resolution box (Ref L0100) was unable to reproduce the H I CDDF (column density distribution function) due to systematically underestimating H I column densities (see fig. 2 of Crain et al. 2017). The authors also found this was largely corrected for in the higher resolution box.

The two models here utilize different values for four key sub-grid parameters (described in table 3 of Schaye et al. 2015), relating to both the stellar feedback, AGN feedback, and the black hole (BH) accretion rate. These were altered for the higher resolution run in order to obtain better agreement with the $z = 0$ GSMF, thereby achieving 'weak convergence' (for a discussion on this see section 2.2 of Schaye et al. 2015) with the standard-resolution run.

During this paper, we also refer to two EAGLE simulations run using a box size of 50 cMpc^3, with/without AGN feedback turned on; RefL0050N0752 and NoAGNL0050N0752, respectively. These simulations are used to isolate the impact of AGN feedback on our results.

2.2 Our sample of galaxies

This work uses the halo catalogue provided by the EAGLE collaboration (McAlpine et al. 2016) in order to identify haloes of interest. These haloes were identified using the Friends-of-Friends (FoF) method (Davis et al. 1985) and SUBFIND algorithms (Springel et al. 2001; Dolag et al. 2009). As in Bahé et al. (2016), we chose to focus our study on central galaxies in order to avoid disentangling the array of environmental processes undergone by satellite galaxies. Such a study is beyond the scope of this paper; however, Marasco et al. (2016) investigated the link between H I and environment for satellite galaxies in EAGLE.

We use the values for R_{200c} (defined as the radius within which density is 200 times the critical density of the Universe) and M_{200c} (the mass within R_{200c}) that were computed using the SUBFIND algorithms. The centre of the halo is taken as the coordinate of the particle with the minimum potential and M_{200c} (also referred to as M_{200} within the paper) is the halo virial mass. We also apply a stellar mass cut of 10^{10} $\mathrm{M}_\odot$ to the galaxies in RefL0100 and a cut of 10^9 $\mathrm{M}_\odot$ to the galaxies in RecalL00025. This ensures the galaxies we study are adequately resolved, particularly when exploring the stellar kinematic morphology of individual galaxies. Throughout the paper all distances quoted in kpc are proper distances (i.e. pkpc), not comoving.

2.3 Calculating galaxy properties

2.3.1 Atomic/molecular hydrogen breakdown

While EAGLE models hydrogen, helium, and nine metals self-consistently, the mass resolution of the simulations is insufficient to follow cold gas to form atoms and molecules (a temperature floor of 8000 K is imposed to avoid artificial fragmentation). Therefore, the ionized/neutral fractions of hydrogen, along with the fraction of molecular hydrogen (H_2) needs to be calculated in post-processing. Our method, detailed in this section, is summarized in Fig. 1. Beyond this, those who are less interested in our detailed H I–H_2 breakdown method can skip to Section 2.3.2, where we go on to talk about our H I kinematic galaxy classifications.

Our method follows previous works (e.g. Lagos et al. 2015, 2016; Bahé et al. 2016; Crain et al. 2017), calculating the H I mass on a particle-by-particle basis, however, we also include modifications based on the method outlined in Diemer et al. (2018). First, the neutral/ionized fraction of hydrogen of each SPH particle was found. To do so, we used the density-dependent fitting function for the photoionization rate of hydrogen given in appendix A1 of Rahmati et al. (2013a). This was formulated based on cosmological simulations between $z = 0$–5 which included radiative transfer (RT) calculations. We linearly interpolate non-integer redshifts, finding our results are insensitive to the linear interpolation method. In their 2013a paper, Rahmati et al. find good agreement between the photoionization rates obtained via post-processing simulations using this best-fitting function and the results of the full RT calculations.

Furthermore, the Rahmati et al. (2013a) fitting formula gives the total photoionization rate, Γ_{pho}, as a fraction of the ionization rate due to background ionizing radiation. We therefore calculated the redshift, temperature, and density-dependent value for the background

Downloaded from https://academic.oup.com/mnras/article/501/3/4396/6041704 by Bodleian Library of the University of Oxford user on 01 April 2021

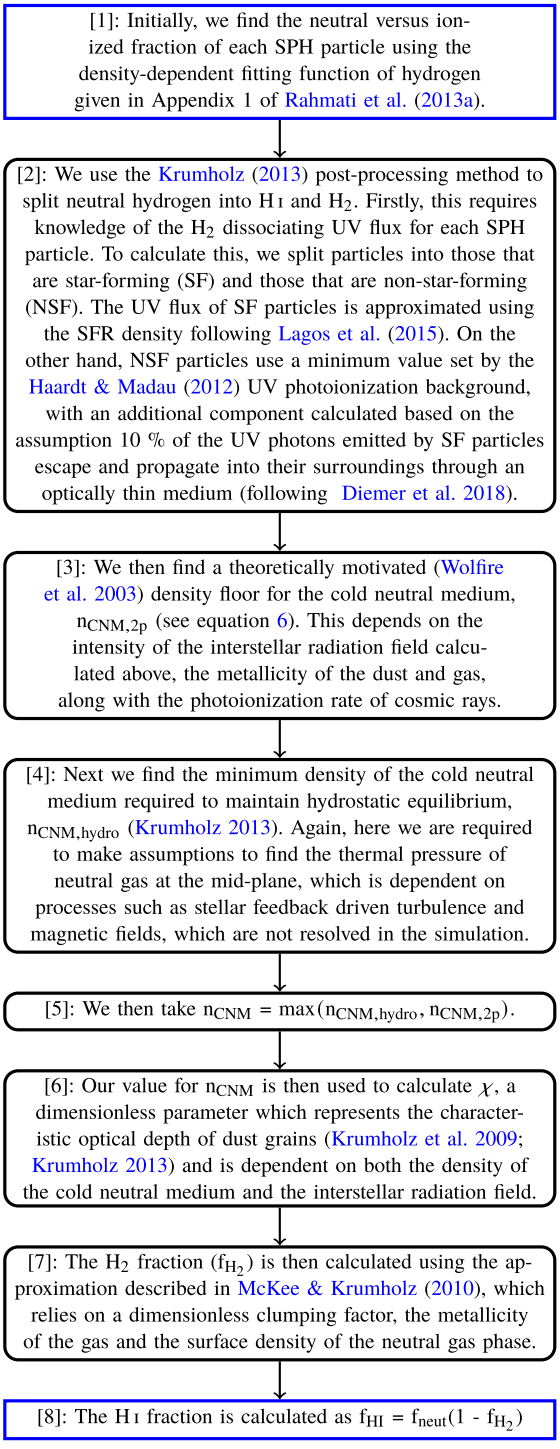


Figure 1. The process of H I/H_2 breakdown, as described in Section 2.3.1.

photoionization rate (Γ_{UVB}) based on the publicly available tables given by Haardt & Madau (2012).[1] These models were calculated using the RT code CUBA (Haardt & Madau 1996, 2001) and represent an updated version of previous models (Madau 1995; Haardt & Madau 1996; Madau, Haardt & Rees 1999). We then used this value of Γ_{UVB}, along with best-fitting parameters linearly interpolated using table A1 of Rahmati et al. (2013a), to calculate Γ_{pho}. This was then fed into the method outlined in appendix A2 of Rahmati et al. (2013a) in order to arrive at the fraction of neutral hydrogen for each gas particle. As in previous works (e.g. Lagos et al. 2015; Crain et al. 2017) we set the temperature of star-forming (SF) particles to 10^4 K, since the temperature of these particles is not physical and instead set by an imposed polytropic equation of state (where $P_{eos} \propto \rho_g^{4/3}$), which limits artificial fragmentation. 10^4 K was chosen to mimic the warm, diffuse ISM surrounding young stellar populations (Crain et al. 2017).

It should be noted that the EAGLE simulations were run using the older photionization rate tables presented in Haardt & Madau (2001). However, we expect this not to affect our results since the gas we are interested in has a column density above that required for self-shielding ($N_{H\,I}$). Moreover, Rahmati et al. (2015) showed that using the Haardt & Madau (2012) model, with its associated reduction in the photoionization rate of hydrogen, improved the agreement between the abundance of H I absorbers in EAGLE and the abundance observed at high redshift ($z = 2.5$).

Rahmati et al. (2013b) showed that local sources of photoionizing feedback have a significant impact on the dense ($N_{H\,I} \sim 10^{18}$–10^{21} cm^{-2}) H I gas distribution in the galaxy. This effect was less significant below $N_{H\,I} \sim 10^{20.5}$ cm^{-2} at the redshift range we are interested in ($z < 1$; see fig. 9 of Rahmati et al. 2013b), however could significantly impact the CDDF of strong DLAs. Furthermore, Rahmati et al. (2013b) found the impact of local stellar radiation (LSR) on strong DLA systems is highly uncertain due to its dependence on the complex morphology of the ISM on local scales. Therefore, although the coupling of the photoionizing radiation from the LSR to DLAs is relevant to this work, it is beyond the scope if this paper. We do, however, take into account the molecular-dissociating radiation associated with LSR and this will be detailed below. Since the photoionizing radiation is not included, we take $N_{H\,I} > 10^{21}$ cm^{-2} as an upper limit. We discuss the prevalence of strong DLAs in our simulations in Sections 3.6 and 4.

There are a number of different post-processing methods previously employed to split neutral hydrogen into H I and H_2 in cosmological simulations. A recent review of the subject is included in Diemer et al. (2018). For the majority of the results in this paper we chose to follow the method outlined in Krumholz (2013), as has been previously utilized for cosmological simulations (e.g. Lagos et al. 2015; Diemer et al. 2018; Stevens et al. 2019a). This prescription divides the neutral atomic H I gas of a galactic disc into a cold ($T < 300$ K) and warm ($T \sim 10^4$ K) phase, alongside a gravitationally bound H_2/molecular phase. It is important to note here that a thermally unstable medium, or UNM, also exists, with spin temperatures of 250–1000 K and constituting 20 per cent of the total H I mass (Murray et al. 2018). However, the inclusion of this phase is beyond the scope of the paper.

Wolfire et al. (2003) showed the cold and hot H I phase can exist in thermal equilibrium across a narrow range of pressures and that the cold neutral ISM (CNM) can have a maximum temperature, $T_{CNM,\,max} \approx 243$ K, which imposes a corresponding density floor, $n_{CNM,\,2p}$, described by

$$n_{CNM,2p} \approx 31 G_0' \frac{Z_d/Z_g}{1 + 3.1(G_0' Z_d/\xi_t')}, \quad (1)$$

where G_0' is the intensity of the interstellar radiation field (ISRF) in units of the Habing radiation field (defined in the wavelength range 912–2400 Å), Z_d and Z_g are the metallicities of the dust and gas, respectively, and ξ_t' is the ionization rate due to cosmic rays and X-rays (Wolfire et al. 2003; Krumholz 2013). Here, for SF gas particles we follow Lagos et al. (2015), where G_0' is approximated as the ratio between the SFR surface density of the gas and the SFR surface density in the solar neighbourhood, which we also take to be 10^{-3}

[1] Available at: http://www.ucolick.org/~pmadau/CUBA/HOME.html.

Downloaded from https://academic.oup.com/mnras/article/501/3/4396/6041704 by Bodleian Library of the University of Oxford user on 01 April 2021

$M_\odot\ yr^{-1}\ kpc^{-2}$. To find Σ_{SFR}, we calculated the SFR density, ρ_{SFR}, using the instantaneous SFR outputted by EAGLE, $\dot{m}_\star$ (equation 1 from Schaye et al. 2015), along with the relation $\dot{m}_\star = m_g(\rho_{SFR}/\rho_g)$. We then multiply ρ_{SFR} by the Jeans length, λ_J, to obtain Σ_{SFR}. Here, λ_J is defined by

$$\lambda_J = \frac{c_{s,eff}}{\sqrt{G\rho_H}}, \tag{2}$$

(Lagos et al. 2015). Where ρ_H is the hydrogen density and $c_{s,\,eff}$ is the effective sound speed, given by

$$c_{s,eff} = \sqrt{\frac{\gamma P_{tot}}{\rho_g}}, \tag{3}$$

(Schaye & Dalla Vecchia 2008) where P_{tot} is the total mid -plane pressure and γ is the ratio of specific heats. In order to calculate γ (and the mean molecular weight μ), both of which are dependent on the atomic-to-molecular ratio (f_{mol}), we follow the iterative method outlined in Stevens et al. (2019a), where

$$\gamma = \frac{5}{3}(1 - f_{mol}) + \frac{7}{5} f_{mol}, \tag{4}$$

and

$$f_{mol} = \frac{X f_{neut}\, f_{H_2}}{1 - Z}, \tag{5}$$

where X is the total hydrogen mass fraction, f_{neut} is the neutral mass fraction calculated above and f_{H_2} is the fraction of the neutral hydrogen which is molecular (Stevens et al. 2019a).

On the other hand, the minimum value of G_0' for each non-star-forming (NSF) particle is set to the UV photoionization background of Haardt & Madau (2012). On top of this, we follow Diemer et al. (2018) by assuming 10 per cent of the UV photons emitted by SF particles escape and propagate through their surroundings via an optically thin medium. This method of modelling the UV strength in NSF particles, detailed in Diemer et al. (2018), avoids a sharp transition between the SF ISM and the NSF ISM. As in Diemer et al. (2018), we used a fast Fourier transform (FFT) technique to convolve the SFR distribution and a $1/r^2$ Green's function using two 128^3 grids – one taking into account the entire galaxy, the second centred on 2 gas half-mass radii – and then interpolated the UV flux at the position of each gas particle. For NSF gas particles inside a given grid cell, a $1/\sqrt{3r_{cell/2}^3}$ contribution from the SFR particles is assumed (Diemer et al. 2018).

Equation (1) is simplified in Krumholz (2013) by making the approximation $Z_d = Z_g$, based on the fact both are attributed to a common supply of metals, along with the substitution $G_0'/\xi_t' = 1$, which relies on the fact both scale with SFR. Performing these substitutions yields

$$n_{CNM,2p} \approx 23 G_0' \left(\frac{1 + 3.1(Z/Z_\odot)^{0.365}}{4.1}\right)^{-1}, \tag{6}$$

(Krumholz 2013). However, equation (6) implies in the absence of an stellar radiation field $n_{min,\,CNM} \to 0$, along with the pressure of the CNM. This unphysical consequence is avoided if one considers the minimum CNM density to maintain hydrostatic equilibrium. Here, the pressure of the neutral gas in the galactic disc ($P_{th,\,disc}$) can be split into three terms describing the self-gravity of the H I which is not bound (1st term), along with the gravitational interaction between the H I and the molecular clouds (2nd term) and the surrounding stars and dark matter (3rd term)

$$P_{th,disc} = \frac{\pi}{2} G \Sigma_{H\,I}^2 + \pi G \Sigma_{H\,I} \Sigma_{H_2} + 2\pi \zeta_d G \frac{\rho_{sd}}{\rho_{mp}} \Sigma_{H\,I}^2, \tag{7}$$

(Krumholz 2013), where ζ_d is taken to be 0.33 and is a dimensionless factor representing the shape of the gas surface density profile, $\Sigma_{H\,I}$ and Σ_{H_2} are surface densities of H I and H_2, respectively, ρ_{sd} is the mid-plane density of stars and dark matter, ρ_{mp} is the volume-weighted mean gas density at the galactic mid-plane. This value is then divided by a factor α in order to find the thermal pressure of the neutral gas at the mid-plane, $P_{th,\,mp}$. This is due to arguments made in Ostriker, McKee & Leroy (2010), motivated by the fact additional supporting processes will be present at the mid-plane, such as stellar feedback-driven turbulence, magnetic fields, and the pressure resulting from thermal gradients caused by cosmic rays. In their paper Ostriker et al. (2010) propose $\alpha = 5$, which is also adopted in Krumholz (2013) and here. Rather than taking a constant value for ρ_{sd} as in previous works (e.g. Crain et al. 2017), we build 1D radial profiles of the stellar and dark matter density for each halo, then interpolate the radius of each gas particle to get the average total stellar and dark matter density at its radius. Diemer et al. (2018) investigate the effects of varying this parameter, finding it can range from 0 to 1 $M_\odot pc^{-3}$. Moreover, Diemer et al. (2018) find by varying ρ_{sd} the mean H_2 masses are similar as those derived using a constant ρ_{sd}; however, the distribution of molecular gas is altered. It is therefore prudent that we do let ρ_{sd} vary, given this paper is primarily concerned with the distribution of the cold gas inside galaxies.

Equation (7) can be re-written using the fact the thermal pressure at the mid-plane can also be expressed in terms of the sound speed of the warm neutral component (WNM), c_w

$$P_{th,mp} = \rho_{mp} \tilde{f}_w c_w^2, \tag{8}$$

where $\tilde{f}_w$ is the ratio of the mass-weighted mean square thermal velocity dispersion to the square of the warm gas sound speed (Krumholz 2013). In this way, the thermal pressure of the gas at the mid-plane can be re-written as

$$P_{th,mp} = \frac{\pi G \Sigma_{H\,I}^2}{4\alpha}\left\{1 + 2R_{H_2} + \left[(1 + 2R_{H_2})^2 + \frac{32\zeta_d \alpha \tilde{f}_w c_w^2 \rho_{sd}}{\pi G \Sigma_{H\,I}^2}\right]\right\}, \tag{9}$$

(Krumholz 2013; Ostriker et al. 2010), where $R_{H_2} = \Sigma_{H_2}/\Sigma_{H\,I}$. This expression for $P_{th,\,mp}$ can be used to form a second constraint on the minimum CNM density (this time labelled $n_{CNM,\,hydro}$)

$$n_{CNM,hydro} = \frac{P_{th,mp}}{1.1 k_B T_{CNM,max}}, \tag{10}$$

which must be met in order to ensure hydrostatic equilibrium. Here, the factor 1.1 is included to account for the contribution of helium. Substituting equation (9) into equation (10), Krumholz (2013) then make the further assumption that the H_2 fraction is $\ll 1$ in this regime, which yields

$$n_{CNM,hydro} \approx \frac{\pi G \Sigma_n^2}{4\alpha(1.1 k_B T_{CNM,max})} \times \left[1 + \left(1 + \frac{32\zeta_d \alpha \tilde{f}_w c_w^2 \rho_{sd}}{\pi G \Sigma_n}\right)^{1/2}\right], \tag{11}$$

where Σ_n is the surface density of the neutral gas. We adopt a value of $\tilde{f}_w = 0.5$, following Ostriker et al. (2010), along with an $\alpha = 5$, $T_{CNM,\,max} = 243$ K, $\zeta_d = 0.33$, and $c_w = 8\,km\,s^{-1}$ (Leroy et al. 2008).

Downloaded from https://academic.oup.com/mnras/article/501/3/4396/6041704 by Bodleian Library of the University of Oxford user on 01 April 2021

Combining equations (6) and (10), we arrive at the following condition for the CNM number density:

$$n_{\rm CNM} = \max(n_{\rm CNM,2p}, n_{\rm CNM,hydro}). \quad (12)$$

The value obtained for $n_{\rm CNM}$ can then be fed into the formalism described in Krumholz et al. (2009) and utilized in Krumholz (2013). In this analytical prescription, the molecular fraction of neutral gas is dependent on the flux of molecule-dissociating far-UV photons, along with the density of dust grains, on the surface of which H_2 molecules can form. Following this prescription, a dimensionless parameter χ can be defined, which represents the characteristic optical depth of the dust

$$\chi = 0.72 G_0' \left(\frac{n_{\rm CNM}}{10\,{\rm cm}^{-3}} \right), \quad (13)$$

(Krumholz 2013). This can then be used to calculate the H_2 fraction (and as a consequence the H I fraction) of the gas, $f_{H_2} = \Sigma_{H_2}/(\Sigma_{H\,I} + \Sigma_{H_2})$, where McKee & Krumholz (2010) showed this can be approximated as

$$f_{H_2} \approx \begin{cases} 1 - (3/4)s/(1 + 0.25s), & s < 2 \\ 0, & s \geq 2, \end{cases} \quad (14)$$

where

$$s \approx \frac{(1 + 0.6\chi + 0.01\chi^2)}{0.6\tau_c}, \quad (15)$$

and

$$\tau_c = 0.066 f_c (Z/Z_\odot) \Sigma_0. \quad (16)$$

f_c is a clumping factor taken to be 5 based on observations by Krumholz & McKee (2005) on the same scales as the minimum spatial resolution of EAGLE and $\Sigma_0 = \Sigma_n / 1\,{\rm M}_\odot\,{\rm pc}^{-2}$.

We note here that our results are robust across different methods of the H I–H_2 breakdown, as is demonstrated in the appendices (see Appendix A). The most significant source of error is the modelling of the galactic feedback processes and chemical enrichment inside the simulation, as will be discussed later in this paper.

2.3.2 *H I kinematics*

In this paper, we investigate the effect $\kappa_{\rm rot,H\,I}$ – the fraction of the kinetic energy of the H I gas that is in ordered rotation – has on the DLA's properties. In order to calculate $\kappa_{\rm rot,H\,I}$, we followed the method outlined in previous works exploring stellar rotation (e.g. Sales et al. 2010; Correa et al. 2017; Thob et al. 2019). Here, we used an aperture of 30 kpc in order to calculate the fraction of the total kinetic energy in H I that is in ordered rotation about the total stellar angular momentum vector, $\hat{z}$, of the galaxy. We did so using the H I fraction per gas particle $f_{\rm H\,I,i}$

$$\kappa_{\rm rot,H\,I} = \frac{\sum^{R<30{\rm kpc}} \frac{1}{2} f_{\rm H\,I,i} m_i \left[L_{z,i}/m_i R_i \right]^2}{\sum^{R<30{\rm kpc}} \frac{1}{2} f_{\rm H\,I,i} m_i v_i^2} \quad (17)$$

(based on equation 1 of Correa et al. 2017). Here, $L_{z,\,i}$ is the angular momentum component of the i-th particle parallel to the total stellar angular momentum vector, and R_i is the projected distance to the stellar angular momentum vector. In this way, $\kappa_{\rm rot,H\,I} = 1$ indicates the H I kinematics in a galaxy is entirely rotation dominated, while $\kappa_{\rm rot,H\,I} = 0$ indicates the H I gas is dispersion dominated. In the top panel of Fig. 2, we plot the histogram of $\kappa_{\rm H\,I}$ at both $z = 1$ (red) and $z = 0$ (blue), combining the resolved galaxies in both the RecalL0025 and RefL0100 simulation boxes to make one histogram. We also include the $z = 0$ and $z = 1$ histograms (solid blue/red histograms,

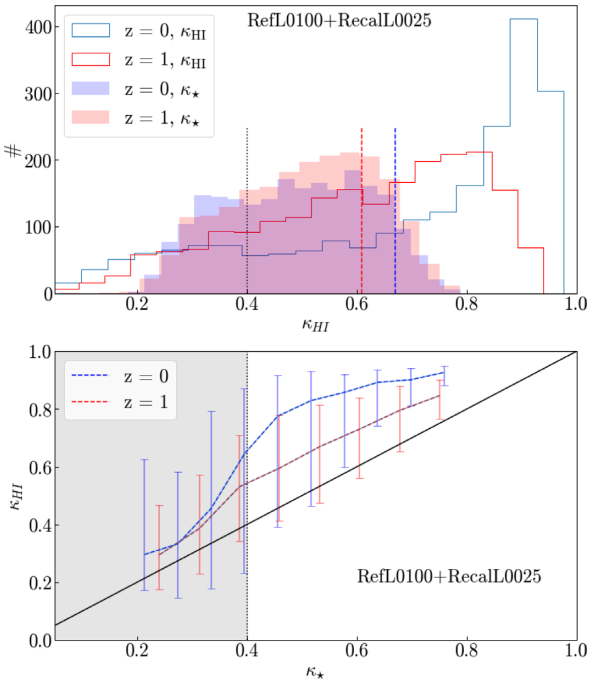


Figure 2. Top plot – the histogram of $\kappa_{\rm H\,I}$ (computed using an aperture of 30 kpc) at both $z = 1$ (red) and $z = 0$ (blue), combining the resolved galaxies in both the RecalL0025 and RefL0100 simulation boxes to make each histogram. The red dashed and blue dashed lines indicate the mean $\kappa_{\rm H\,I}$ values in our $z = 1$ and $z = 0$ samples, respectively. The dotted vertical line indicates the boundary between dispersion-dominated and rotation-dominated stellar kinematics used in Correa et al. (2017). The shaded blue and red histograms indicates the $z = 0$ and $z = 1$ $\kappa_\star$ distributions of our galaxy samples. Lower plot – $\kappa_{\rm H\,I}$ versus $\kappa_\star$ for our sample of resolved galaxies taken from both the RecalL0025 and RefL0100 simulation boxes, at $z = 0$ (blue) and $z = 1$ (red). The 16th–84th percentile ranges are indicated by the capped vertical lines. The shaded region indicates the $\kappa_\star$ range that is considered to be dispersion-dominated in Correa et al. (2017). The solid line indicates a one-to-one relationship.

respectively) of $\kappa_\star$ (the rotational energy fraction of the stars), again using both boxes, calculated using the same method as the H I, along with the mean $\kappa_{\rm H\,I}$ values at each redshift. Here, we can see the $\kappa_{\rm H\,I}$ distribution is skewed towards 1 at $z = 0$, and to a lesser extent at $z = 1$. We have also plotted a vertical dotted line at $\kappa = 0.4$, which represents the boundary between dispersion-dominated and disc-dominated stellar kinematics used in Correa et al. (2017). Comparing the $z = 0$ $\kappa_{\rm H\,I}$ and $\kappa_\star$ histograms, we can see that $\kappa_{\rm H\,I}$ is more extended, with a mean value of 0.67, as opposed to 0.48 for the stars. This difference is lessened at $z = 1$, where the mean values of the H I and stellar distributions are 0.6 and 0.5, respectively.

We investigate the relationship between stellar and H I kinematics further in the lower plot of Fig. 2, where we plot $\kappa_{\rm H\,I}$ against $\kappa_\star$, again combining the resolved galaxies from the two simulation boxes, RecalL0025 and RefL0100. The grey region highlights the area where $\kappa_\star \leq 0.4$. The black solid line indicates a one-to-one relationship. The $\kappa_{\rm H\,I}$ values are systematically higher than the corresponding $\kappa_\star$ value for a given galaxy at $z = 0$ and $z = 1$, while the $z = 0$ galaxies show a distinctly non-linear relation between the two quantities; with a steep gradient between $\kappa_\star = 0.2$–0.5 and a shallower gradient beyond this. Since there is no clear transition point between two kinematic populations of galaxies at $z = 1$ (either in the H I or stars) we use the mean of the $\kappa_{\rm H\,I}$ values of our sample, 0.6, to be our transition point between dispersion-dominated ($\kappa_{\rm H\,I} < 0.6$)

Downloaded from https://academic.oup.com/mnras/article/501/3/4396/6041704 by Bodleian Library of the University of Oxford user on 01 April 2021

and rotation-dominated ($\kappa_{\rm H\,I} \geq 0.6$) H I kinematics. At $z = 0$, we instead use the higher threshold of $\kappa_{\rm H\,I} \geq 0.67$ for $z = 0$, given this is the mean value of the distribution.

We explored the effect of altering the aperture by re-plotting Fig. 2, with an aperture of 50 kpc for the H I instead (not shown for brevity). We found that increasing the aperture decreases the mean of the $z = 0$ and $z = 1$ $\kappa_{\rm H\,I}$ distributions to $\geq$0.55, while the $z = 1$ $\kappa_{\rm H\,I}$–$\kappa_\star$ relation moves away from the 1:1 line towards higher $\kappa_{\rm H\,I}$ values for a given $\kappa_\star$. Despite these differences, the overall trends are similar – the $z = 0$ $\kappa_{\rm H\,I}$ distribution showed a significant skew towards higher $\kappa_{\rm H\,I}$ values when compared with the $z = 1$ distribution, while the $\kappa_{\rm H\,I}$ value of galaxies increased with $\kappa_\star$ at both redshifts using both apertures, with the H I showing a significantly higher rotation to total kinetic energy ratio than the stars.

2.3.3 *Measurements of DLAs*

We use three different methods to estimate the distribution of high column density gas associated with each galaxy. The first two involve taking the covering fraction, $f_{\rm cov}$, of each galaxy. To do so, we orient the galaxy face-on (using its total stellar angular momentum axis) and use SPH interpolation to project it on to a 2D grid. In our fiducial method, based on Nagamine, Springel & Hernquist (2004), the grid has a length of 2 $R_{\rm 200c}$ (centred on the minimum of the potential well of the galaxy) and is made up of n^2 grid cells. Here, n was chosen to ensure a cell size of 3 kpc (approximately four times the softening length, 0.7 pkpc). We also varied this from 2 to 5 kpc, finding this had an insignificant effect on our results. We then find the H I column density ($N_{\rm H\,I}$) associated with each 2D grid cell by summing over all particles that meet three spatial criteria: an x-position inside the defined cell, a y-position in the defined cell, and a z-position within $2R_{\rm 200c}$

$$N_{\rm H\,I} = \frac{L_{\rm cell}}{m_{\rm p}} \sum_{\rm i} \rho_{\rm H\,I,i}, \tag{18}$$

where $m_{\rm p}$ is the mass of a proton, $L_{\rm cell}$ is the length of each grid cell, and $\rho_{\rm H\,I}$ is the SPH interpolated H I density of each cell. $f_{\rm cov}$ is then defined as the fraction of the total number of grid cells with $N_{\rm H\,I} > 10^{20.3}$ cm^{-2}. A second covering fraction, $f_{\rm cov,\,70\,kpc}$ was also defined using a fixed grid length of 140 kpc, independent of the size/mass of the system.

Finally, volume filling fractions, $f_{\rm vol}$, were also computed using a 3D grid containing n^3 cells and a grid size of $2R_{\rm 200c}$. This time the column density per cell was defined as $(\rho_{\rm H\,I}/m_{\rm p})L_{\rm cell}$ and the covering fraction was calculated as the number of cells with $N_{\rm H\,I} > 10^{20.3}$ cm^{-2} divided by the total number of cells. The volume filling fractions allow us to gauge the 3D distribution of the high column density H I about a galaxy, for example should a galaxy have a high volume filling fraction and a low covering fraction, this would imply a highly disturbed DLA distribution. Moreover, the individual cells used for the volume filling factors allow us to understand the local properties of individual DLAs in a way that is not possible averaging over a column.

To illustrate our method, we plotted two examples of the 2D $N_{\rm H\,I}$ grids obtained using a total grid side length of 200 kpc for two galaxies extracted from the EAGLE RefL0100 simulation at $z = 0$ (upper plots of Fig. 3). The left plot was obtained for a galaxy with dispersion-dominated stellar kinematics, while the lower plot was obtained for a galaxy with a high stellar rotation-to-dispersion kinematic ratio. As expected the late-type galaxy has higher covering and volume filling factors, and, due to projections, the covering fraction is usually higher than the volume filling fraction.

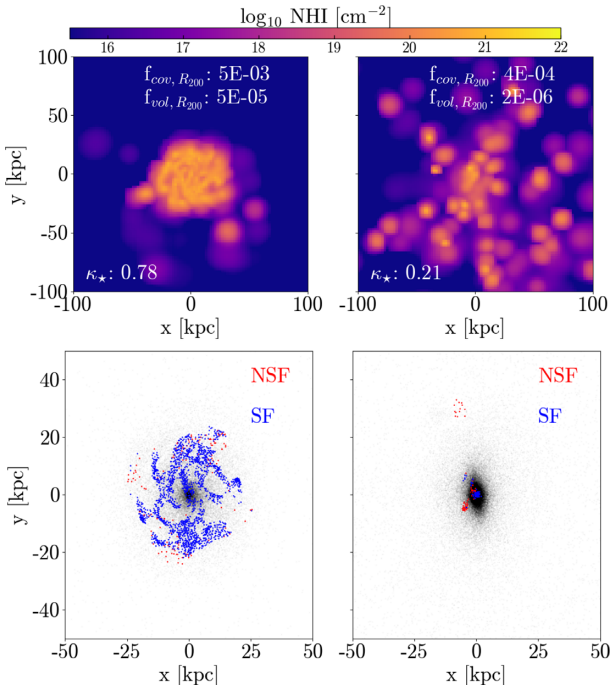


Figure 3. Upper row – 2D gridding of two galaxies taken from the EAGLE RefL0100 simulation at $z = 0$. The galaxy on the right has a low stellar rotation-to-dispersion kinematic ratio ($\kappa_\star$), while the galaxy on the left is rotation-dominated. Plots are orientated face-on. The 2D face-on DLA covering fraction ($f_{\rm cov,R_{200}}$) and 3D volume filling fraction for DLAs ($f_{\rm vol,R_{200}}$), calculated using an aperture equal to virial radius ($R_{\rm 200c}$) of each galaxy, are shown on each plot, along with the $\kappa_\star$ values. Lower row – the application of the Mitchell et al. (2018) ISM selection criteria to the same two galaxies, zooming in to the central 50 kpc of each galaxy. The SF ISM gas particles are shown in blue, while the NSF particles are in red. Black points represent the position of star particles.

2.4 ISM versus CGM

We further split the grid cells into those containing gas associated with the ISM and those that do not, categorizing the latter as CGM sightlines and the former as ISM sightlines. To class individual particles as being exclusively part of the CGM or ISM, we used the method outlined in Mitchell et al. (2018). This method computes whether or not a gas particle is rotationally supported, along with its temperature and position within the galaxy. To be in the ISM, the particle has to satisfy the following criteria:

(i) The temperature of the gas particle must be below 10^5 K, unless the hydrogen number density, $n_{\rm H}$, is greater than 500 cm^{-3}.

(ii) The gas must be dense, with $n_{\rm H} > 0.03$ cm^{-3}, or be rotationally supported. The latter requires the gas to satisfy the following numerical criteria:

$$-0.2 < \log_{10}\left(\frac{2\epsilon_{\rm k,rot}}{\epsilon_{\rm grav}}\right) < 0.2, \tag{19}$$

and

$$\frac{\epsilon_{\rm k,rot}}{\epsilon_{\rm k,rad} + \eta_{\rm th}} > 2, \tag{20}$$

where $\epsilon_{\rm k,\,rot}$ is the specific kinetic energy of the particle that is attributed to rotation about the galactic centre, $\epsilon_{\rm k,\,rad}$ is the same but for radial motion, $\epsilon_{\rm grav}$ is the specific gravitational energy of the particle ($GM(r)/r$), and $\epsilon_{\rm th}$ is the specific internal energy of the particle.

Downloaded from https://academic.oup.com/mnras/article/501/3/4396/6041704 by Bodleian Library of the University of Oxford user on 01 April 2021

(iii) The radial distance of the gas particle to the galaxy centre must be below 0.5 R_{200c}.

Furthermore, following Mitchell et al. (2018), once the ISM particles have been selected, any gas particles at a radius greater than r_{90} (the radius enclosing 90 per cent of the ISM mass) are considered CGM instead, while if the galaxy has a $M_{ISM}/M_\star$ ratio of less than 0.1, any gas particles beyond 5 $r_{1/2}$ are also considered to be CGM.

The results of applying the above set of criteria to the galaxies of the top panels of Fig. 3 are shown on the bottom row. Here, we have zoomed in to the central 50 kpc region of each galaxy; the SF ISM particles are plotted in blue and the NSF ISM particles are coloured red. The star particles are shown as black points in the background.

These methods allow an in-depth exploration of the distribution of H I inside a galaxy. In particular, we compare high column density H I in the ISM with the CGM.

3 RESULTS

3.1 Mass scaling relations and evolution with redshift

Initially, we investigate the redshift evolution of the global H I budget of haloes in order to understand the typical H I properties of galaxies and their surroundings in the redshift range probed by FLASH. In particular, we are interested in the spatial distribution/kinematics of the H I in these galaxies and to understand what a typical H I mass-selected galaxy looks like at $z = 1$. Fig. 4 shows the $M_{H I}$–$M_\star$ relation for both the RefL0100 and RecalL0025 galaxy samples at varying redshift. Also plotted are the estimates of Catinella et al. (2018), from targeted H I observations of a stellar-mass selected sample at $z \approx 0$. This survey comprises of 1179 galaxies in the local Universe. We compute the median $M_{H I}$–$M_\star$ relation for a representative sample[2] of the xGASS central galaxies (dashed lines). Here, we initially calculated the H I mass using all gas particles attributed to the halo using SUBFIND (our methods are explored later in the section). At $z = 0$, the H I masses obtained using the larger box are systematically lower than those obtained at the same stellar mass for the higher resolution box. On further analysis, we found there was no significant difference in the median cold gas fractions measured for both simulation boxes at $z = 0$, the difference in H I masses is instead driven by the relative abundances of H_2 and H I. As was also seen in Lagos et al. (2015), the galaxies inside the RefL0100 EAGLE simulation have systematically higher ISM mean metallicities (a fact that will also become important when considering the properties of associated DLAs, see Section 3.3) and since the post-processing H I prescription relies on dust as a catalyst of H_2 formation, which we explicitly link to metallicity (see Section 2.3.1), this results in higher M_{H_2}/M_{neut} ratios (where M_{neut} is neutral gas mass; for a discussion on this see section 4.1 of Lagos et al. 2015). This effect is present both a $z = 0$ and $z = 1$, but is more significant at lower redshift.

We also investigated how the relative metallicity of the H I gas in the galaxies changes with radius in the RefL0100 and RecalL0025 simulations, in order to further understand the disparity seen in the H I masses between the different boxes at $z = 0$, along with why this disparity disappears at higher redshift. We measured the mean neutral-mass-weighted metallicity (Z_{neut}) of all gas below 2 different radii; 0.1 R_{200c} and 2 R_{200c}. We plot this for $z = 1$ and $z = 0$ in Fig. 5. At both redshifts, the disagreement between the mean metallicities in the two EAGLE simulations is more pronounced when averaging

[2]https://xgass.icrar.org/data.html.

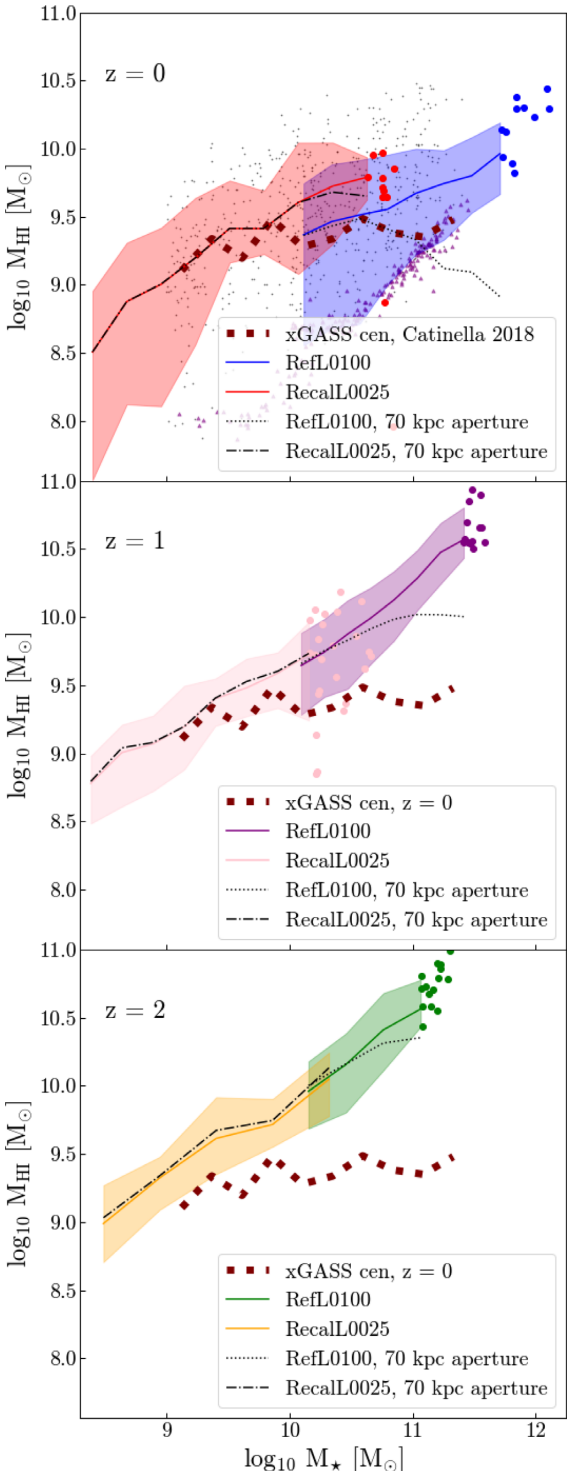


Figure 4. The $M_{H I}$–$M_\star$ relation at $z = 0$ (top row), $z = 1$ (middle row), and $z = 2$ (bottom row), as calculated for both EAGLE box RecalL0025 and RefL0100. The solid lines indicate the median values in 10 stellar mass bins for each galaxy sample, while the shaded regions are the 16th–84th percentile range inside each stellar mass bin. Points indicate galaxies in stellar mass bins containing fewer than 10 galaxies. Also plotted is a representative sample of the $M_{H I}$ and $M_\star$ values obtained by the xGASS survey (Catinella et al. 2018) (black dots/purple triangles for detections/non-detections), along with the median values for central galaxies (dashed line). We overplot the $M_{H I}$–$M_\star$ relation obtained using a 70 kpc aperture for the H I gas for both the RefL0100 run (black, dotted line) and the RecalL0025 run (black, dot–dashed line).

Downloaded from https://academic.oup.com/mnras/article/501/3/4396/6041704 by Bodleian Library of the University of Oxford user on 01 April 2021

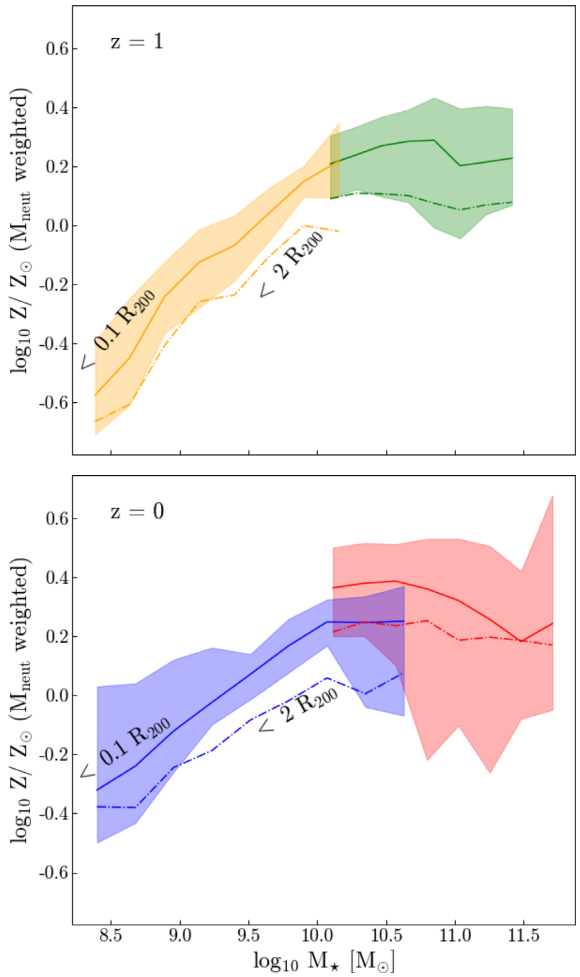


Figure 5. The mean metallicity, weighted by the neutral gas mass $M_{\rm neut}$, calculated for all gas below 2 radii; 0.1 $R_{\rm 200c}$ (solid lines) and 2 $R_{\rm 200c}$ (dot–dashed lines) as a function of stellar mass, for galaxies in the RefL0100 (blue/green) and RecalL0025 (red/orange) EAGLE simulations at $z = 1$ (upper plot) and $z = 0$ (lower plot). The shaded areas show the 84th–16th percentile range.

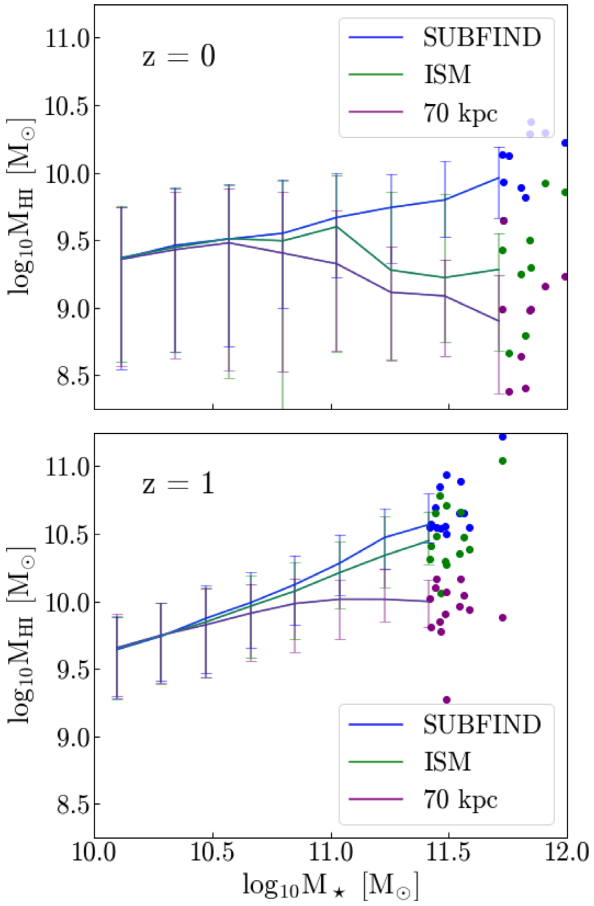


Figure 6. The $M_{\rm H\,I}$–$M_\star$ relation at $z = 0$ (upper plot) and $z = 1$ (lower plot) for the RefL0100 galaxy sample, with three different methods of calculating the H I mass indicated. 'SUBFIND' indicates all gas particles attributed to a halo are used to calculate the H I mass, while '70 kpc' indicates all gas particles within a 70 kpc radius and 'ISM' uses just the H I mass attributed to the ISM using the method described in Section 2.4. The values for stellar mass bins that contain less than 10 galaxies are shown as points, while the 16th – 84th percentiles are indicated by the vertical lines.

over the entire galaxy. This disagreement is also seen when averaging over all gas particles below 0.1 $R_{\rm 200c}$ for $z = 0$. On the other hand, at $z = 1$, the two resolution boxes show a good agreement for the mean neutral-mass-weighted metallicities below 0.1 $R_{\rm 200c}$ for galaxies in the same stellar mass bin.

The better agreement between metallicities in the inner parts of the galaxy, where H_2 is primarily expected to form, results in the better agreement between H_2 and H I mass fractions in the centre of galaxies at $z = 1$. Furthermore, the systematic increase in the metallicity of the neutral gas in the outer parts of the galaxy, or the CGM, does not have a significant impact on the molecular/atomic decomposition, since this gas is at temperatures and pressures that prohibit the formation of H_2. We also see this result when comparing the SF and NSF gas metallicities between the two EAGLE boxes, finding the agreement between the $Z_{\rm NSF}$ values is better at low z, while the opposite is true for the SF gas (we have not included this plot for brevity).

Focussing again on Fig. 4, our fiducial $z = 0$ RefL0100 results do not show the downturn seen in the $M_{\rm H\,I}$–$M_\star$ relation at $z = 0$ by Crain et al. (2017) also using EAGLE. This is due to the fact the latter utilize a 70-kpc aperture, while we consider all gas associated with the galaxy via SUBFIND when determining H I masses. According to the H I size–mass relation (known to be extremely robust, see Stevens et al. 2019b, and references therein), we would expect galaxies with H I masses above $10^{10.8}$ M$_\odot$ to have a significant fraction of their H I extending beyond 70 kpc and indeed we do see that the use of the 70-kpc aperture has the largest impact at high $M_\star/M_{\rm H\,I}$. However, Fig. 4 shows a significant reduction in the H I mass measured using a 70-kpc aperture at H I masses of $>10^9$ M$_\odot$ (or alternatively $M_\star > 10^{10}$ M$_\odot$) at $z = 0$. This discrepancy in H I mass is seen at all redshifts (however is greatest at $z = 0$) and implies a significant mass of H I lies outside the galactic disc (i.e. in the CGM) of systems with $M_\star > 10^{10}$ M$_\odot$ at $z = 0$, or $M_\star > 10^{10.5}$ M$_\odot$ at $z = 1$.

When we plot the ISM H I masses computed as detailed above, we see the H I masses are reduced substantially, particularly at $z = 0$. This is demonstrated in Fig. 6 where we show the $M_{\rm H\,I}$–$M_\star$ relation at $z = 0$ and $z = 1$ plotted for the RefL0100 galaxy sample using different methods of calculating the H I mass. At both redshifts, using just the H I associated with the ISM reduces the H I masses calculated (albeit to a lesser extent at $z = 1$) indicating that a significant mass of H I is in the CGM of higher mass galaxies at $z = 0$.

Downloaded from https://academic.oup.com/mnras/article/501/3/4396/6041704 by Bodleian Library of the University of Oxford user on 01 April 2021

We find the $M_{\rm H\,I}$–$M_\star$ relation shows an increase in normalization in both the reference and re-calibrated box as redshift increases (more noticeable for the RefL0100 run). This can be seen clearly by comparing the offset of the median $M_{\rm H\,I}$–$M_\star$ profile (solid lines) to the median of the xGASS galaxies (dashed lines) in Fig. 4. The offset from the $z = 0$ $M_{\rm H\,I}$–$M_\star$ relation increases with $M_\star$ in both simulation boxes.

Both RefL0100 and RecalL0025 agree well with the observations at $z = 0$ within the stellar mass range adopted here. This gives us confidence that we can use EAGLE to explore the ISM and CGM H I content of galaxies and haloes.

3.2 The covering fraction of DLAs as a function of galaxy properties

Now that we have explored the global H I scaling relations, and in particular inferred the presence of a significant H I mass outside the galactic disc of high-mass galaxies, we will dive into the key results of the paper: the redshift evolution of DLA properties, along with the properties of their host haloes. We begin by investigating the distribution of DLAs inside galaxies using the 2D covering fractions ($f_{\rm cov,R_{200}}$; for details on how these were calculated refer to Section 2.3.3).

The top panel of Fig. 7 shows $f_{\rm cov,R_{200}}$ as a function of M_{200} for the EAGLE RefL0100 (solid lines) and the RecalL0025 (dotted lines) simulations. Both boxes show a redshift evolution in the median covering fraction, with higher values at higher redshift.

Focussing on $z = 0$, we can see that between $10^{11.5}$ M$_\odot$ $< M_{200} \leq$ 10^{12} M$_\odot$, $f_{\rm cov,R_{200}}$ increases with halo mass, but there is a turnover at $\sim 10^{12.25}$ M$_\odot$. This turnover is present in both simulation boxes and in the same halo mass range. On the other hand, at $z = 1$, $f_{\rm cov,R_{200}}$ is close to flat and independent of M_{200}.

We have also included the $z = 2$ values in Fig. 7 in order to ascertain whether the $f_{{\rm cov},R_{200}}$–M_{200} trends remain flat at higher redshift. Instead, we see the $f_{{\rm cov},R_{200}}$–M_{200} relation is inverted at $z = 2$ compared with $z = 0$; $f_{{\rm cov},R_{200}}$ increases with increasing M_{200} in both the RefL0100 and RecalL0025 EAGLE simulations, albeit weakly. Overall, these results indicate a complex, non-linear relationship between halo mass and DLA covering fractions, with the covering fractions of high-mass ($M_\star > 10^{11}$ M$_\odot$) galaxies becoming more significant at higher redshift. This is most likely due to the fact the vast majority of galaxies at $z = 2$ are actively forming stars, as opposed to $z = 1$, where galaxies at higher M_{200} become more passive.

The position of the turnover at $z = 0$ corresponds to the turnover in the GSMF seen both observationally (e.g. Tomczak et al. 2014; Davidzon et al. 2017) and theoretically (e.g. Beckmann et al. 2017) when AGN feedback is accounted for. This could imply that AGN feedback is acting to reduce the H I with DLA-like column densities into a lower column density phase. Or alternatively, the inefficiency of stellar feedback at driving gaseous outflows in high-stellar-mass galaxies is also likely to reduce the H I covering fraction. Furthermore, this turnover could also signify an increase in the clumpiness, or H I-mass-weighted density, of DLAs (we discuss this further in Section 3.6).

We test the impact of AGN feedback on the trends in the DLA covering fraction – M_{200} relation seen in Fig. 7 by re-plotting the $z = 0$ results for an EAGLE simulation with/without AGN feedback included; RefL0050N0752 (in blue) and NoAGNL0050N0752 (in red), respectively, controlling for stellar mass instead of halo mass (Fig. 8). Here, we see both simulations show a downturn in the DLA covering fraction at high stellar masses, but this occurs at a stellar mass that is ∼0.5 dex higher when AGN feedback is not included. This supports our conclusion that AGN feedback is acting to reduce the DLA covering fraction of high-mass galaxies. Although, this effect becomes insignificant beyond a stellar mass of $\sim 10^{11}$ M$_\odot$.

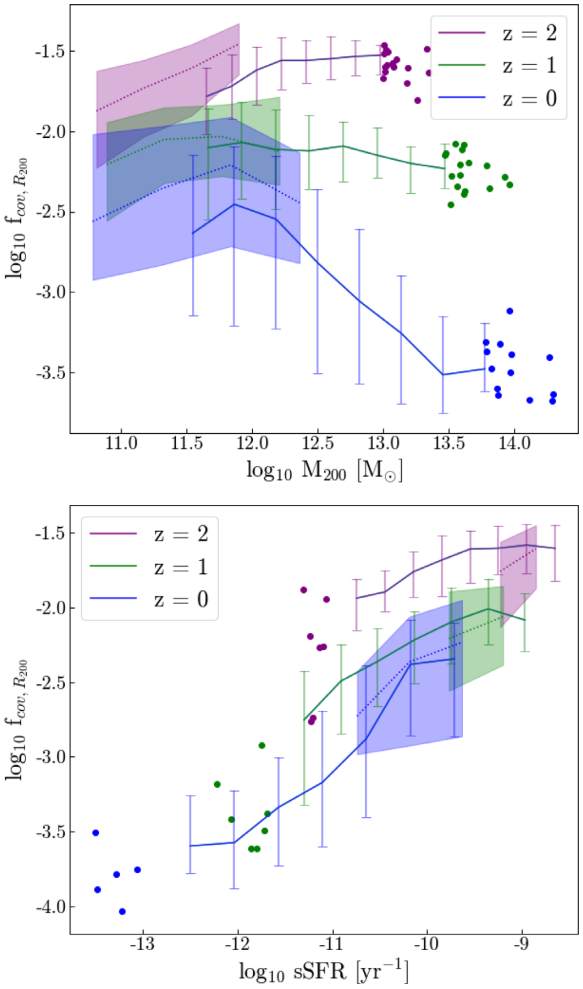


Figure 7. The DLA covering fraction as a function of M_{200} (top plot), sSFR (defined as SFR/$M_\star$, lower plot) at $z = 2$ (purple), $z = 1$ (green), and $z = 0$ (blue). The median values for the sample of galaxies taken from the EAGLE RefL0100 simulation are shown using the solid lines, while those from the RecalL0025 are shown using dotted lines. The 84th–16th percentile range is indicated by the vertical lines for the RefL0100 simulation and the shaded area for the RecalL0025 galaxies. Where bins contain fewer than 10 galaxies, individual galaxies are plotted as points.

It is also possible the transition of the high density H I associated with DLAs into molecular hydrogen is more efficient in systems with halo mass greater than 10^{12} M$_\odot$, while the cooling of the cold gas is less efficient. We plot the gas phase diagram of the gas particles in galaxies with $M_{200} > 10^{13}$ M$_\odot$ and $M_{200} < 10^{12}$ M$_\odot$ in Fig. 9, colouring the particles according to their H I gas mass fraction ($M_{\rm H\,I}/M_{\rm gas}$). Here, we see the characteristic equation of state ($T \propto {n_{\rm H}}^{1/3}$; applied to avoid artificial fragmentation as a power law) in the lower right of each panel. It is this gas that will be SF. Concentrating on the particles with the highest H I mass fraction in red, the shaded rectangle highlights the fact the high halo mass galaxies have a large mass of H I in the temperature range of 10^4–10^5 K, at intermediate density ($n_{\rm H} = 10^{-2}$–10^0 cm^{-3}). This indicates an additional heating source of the diffuse H I in the latter case, such as AGN.

Downloaded from https://academic.oup.com/mnras/article/501/3/4396/6041704 by Bodleian Library of the University of Oxford user on 01 April 2021

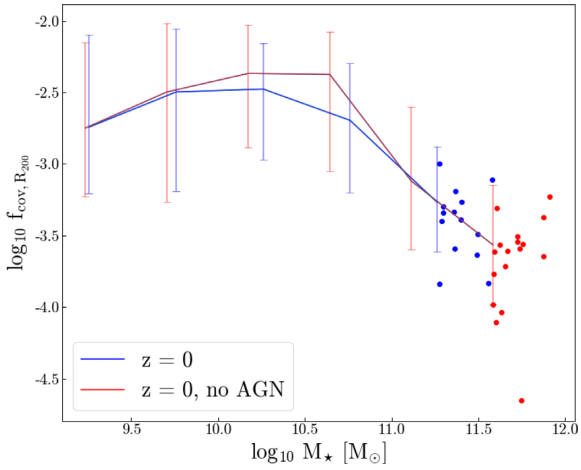


Figure 8. The DLA covering fraction as a function of $M_\star$ at $z = 0$. The median values for the sample of galaxies taken from the EAGLE RefL0050N0752 simulation are shown using the blue solid lines, while those from the NoAGNL0050N0752 are shown in red. The 84th–16th percentile range is indicated by the vertical lines. Where bins contain fewer than 10 galaxies, individual galaxies are plotted as points.

Additionally, in the lower right of the plot (in the area marked by the shaded blue circle) we can see the H I fraction in SF gas (i.e. the gas lying in the imposed equation of state) is significantly higher in the bottom panel compared to the top panel, indicating that while there is an effective source of heating in the higher mass galaxies, there is also a significant build up of high density, SF gas. This heating/SF gas build-up is in line with results from Bower et al. (2017), who ascribed it to the suppression of star formation-driven outflows in the hot corona of massive galaxies, leading to a build up of gas in the central regions of the galaxy and a subsequent period of non-linear black hole growth and intense AGN feedback. This then heats the corona and prevents further cold gas accretion on to these galaxies.

Focussing on what these results mean for FLASH, the trends in covering fraction seen here link directly to both the probability of high/low impact parameters for given galaxies, along with the probability of an intervening absorption detection should each galaxy be situated along a given sightline. The higher covering fractions we see at $z = 1$ link to the recent finding of a high impact parameter absorption detection in an early-type galaxy at redshift $z = 0.3562$ in Allison et al. (2020). Our results suggest higher impact parameter (relative to the size of the galaxy halo) absorption detections are more likely the further you look back in redshift.

There is a clear positive correlation between the DLA covering fraction and sSFR (lower panel of Fig. 7) and H_2 mass fraction (calculated as M_{H_2}/M_{200}, not shown in figure for brevity) at $z = 0$, $z = 1$, and $z = 2$, indicating that galaxies with higher sSFR also have a more extended distribution of DLAs, relative to R_{200c}. This correlation is steepest at $z = 0$ and the gradient is reduced at higher redshift. Consequently, the higher redshift DLAs in EAGLE are attributed to galaxies with a wider range of sSFRs at $z = 1$ and $z = 2$. This hints that H I absorption surveys such as FLASH will be tracing a representative sample of galaxies at $z = 1$ (although this is contingent on the CNM covering fraction following the same trends as that of the DLAs).

The relationship between $\kappa_{H\,I}$ and the H I covering fraction is explored in Fig. 10, where the median covering fraction is skewed to significantly higher values for galaxies with high $\kappa_{H\,I}$ values at $z =$

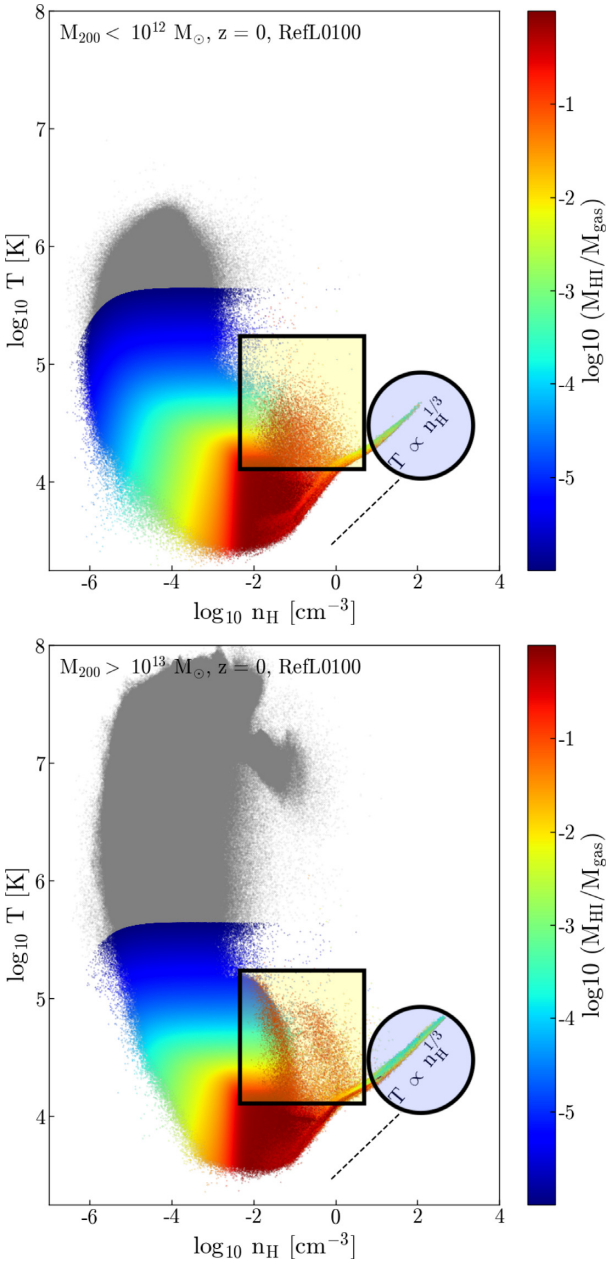


Figure 9. Temperature versus hydrogen number density (n_H) plots for the gas particles, coloured by H I mass fraction, in galaxies of halo mass $< 10^{12}$ $M_\odot$ (top plot) $> 10^{13.5}$ $M_\odot$ (lower plot) taken from the RefL0100 simulation at $z = 0$. All other gas particles associated with the galaxies are included as grey points. The rectangles and circles highlight areas of interest. The $T \propto n_H^{1/3}$ line indicates the equation of state imposed in EAGLE to avoid artificial fragmentation below the resolution limit.

1. Here, we used the rotation/dispersion-dominated classification detailed in Section 2.3.2. In other words, at this redshift, the DLA covering fraction is greater for H I discs than for dispersion-dominated H I morphologies. We find that there is good agreement between the median $f_{cov,R_{200}}$ values at $z = 1$ in different EAGLE boxes for both kinematic populations. From Fig. 10, we can see at $z = 0$, our galaxy sample is dominated by galaxies with low covering fractions even in the sub-sample of $\kappa_{H\,I} \geq 0.67$ galaxies. However, the latter displays a higher covering fraction tail that is not present for the dispersion-dominated galaxies. This tail is more prominent for

Downloaded from https://academic.oup.com/mnras/article/501/3/4396/6041704 by Bodleian Library of the University of Oxford user on 01 April 2021

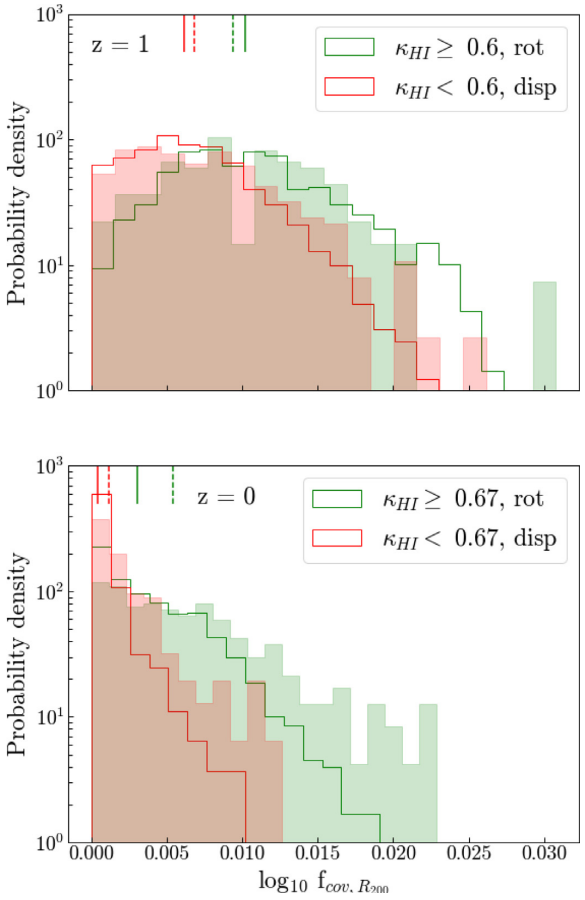


Figure 10. The probability density distribution of $f_{\mathrm{cov},R_{200}}$ values for galaxies taken from RefL0100 (step histograms) and RecalL0025 (shaded histograms) at $z = 0$ (lower plot) and $z = 1$ (upper plot), then split into two bins according to their $\kappa_{\mathrm{H\,I}}$ values, with galaxies with rotation-dominated H I kinematic morphologies in green and those with dispersion-dominated H I kinematics in red (following the categorization detailed in Section 2.3.2). The median $f_{\mathrm{cov},R_{200}}$ values for the RefL0100 (RecalL0025) sample are shown as solid (dashed) lines at the top of the plot, with red lines indicating the dispersion-dominated galaxy population and the green lines indicating the rotation-dominated galaxies.

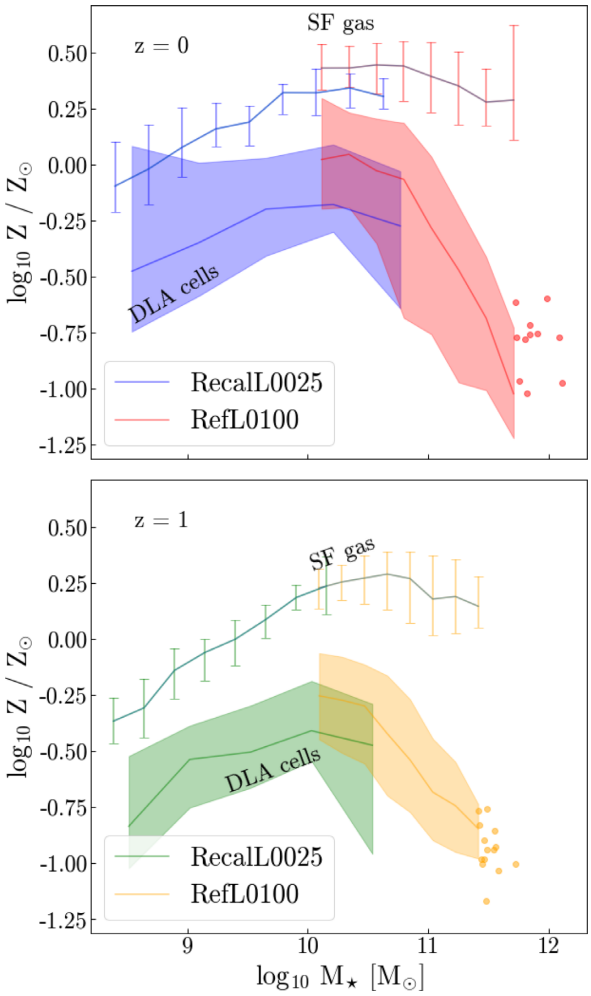


Figure 11. The mean DLA metallicity (calculated using 3D cells, see Section 2.3.3) as a function of $M_\star$ at $z = 0$ (upper plot) and $z = 1$ (lower plot) for the RefL0100 (red and orange) and RecalL0025 (blue and green) EAGLE simulations. The solid lines are the median values for both simulations, while the 16th–84th percentile regions are indicated by the shaded regions. We have also included the median values of the metallicity of the SF gas in central galaxies for the different stellar mass bins (following the same colour scheme), again with the 16th–84th percentile ranges shown as vertical lines.

the sample of galaxies taken from the RecalL0025 EAGLE box. Also, the median $f_{\mathrm{cov,R_{200}}}$ values are systematically higher in RecalL0025 compared with the RefL0100 simulation.

Overall, from Fig. 10 we know that the higher covering fractions/higher relative impact parameters DLAs seen in Fig. 7 are likely to be associated with rotationally dominated H I morphologies, supporting the hypothesis that the absorption detection in Allison et al. (2020) was associated with a large H I disc.

In the next section, we will explore the properties of the DLAs themselves and how these vary with z.

3.3 Investigation of DLA properties

We plot the mean metallicities of the DLA grid cells used in the calculation of f_{vol} (see Section 2.3.3), against the stellar mass of galaxies in our sample in Fig. 11. We have also included the mean metallicity of SF gas in each galaxy as a reference. The mean metallicity of the DLA grid cells follows the same trends as the total gaseous component of the galaxies; the higher resolution simulation has systematically lower metallicities than RefL0100. Furthermore, there is an apparent disparity in the trends at low stellar mass ($<10^{10}$ $\mathrm{M_\odot}$) and high stellar mass ($>10^{10.5}$ $\mathrm{M_\odot}$). Regardless of redshift, galaxies with $M_\star < 10^{10}$ $\mathrm{M_\odot}$ have DLA metallicities that show a gradual increase with $M_\star$. Both boxes show a turnover between 10^{10} and $10^{10.5}$ $\mathrm{M_\odot}$ and a subsequent negative correlation between $Z_{\mathrm{vol},R_{200}}$ at higher stellar mass. The mean metallicity of the DLA cells is uniformly lower than that of the SF gas, but this disparity increases with stellar mass at both redshifts.

These results hint that DLAs in high- and low-mass galaxies may trace different galaxy evolutionary processes – for example, the relatively metal-poor DLAs in the low-stellar-mass ($<10^9$ $\mathrm{M_\odot}$) galaxies are likely to be associated with the smooth accretion of low-metallicity gas, while higher metallicity DLAs in galaxies with $M_\star \sim 10^{10}$ $\mathrm{M_\odot}$ could be associated with enrichment via stellar feedback, the re-accretion of recycled gas or the accretion of metal-rich material from galaxy mergers. Previous works suggest the dominant accretion

Downloaded from https://academic.oup.com/mnras/article/501/3/4396/6041704 by Bodleian Library of the University of Oxford user on 01 April 2021

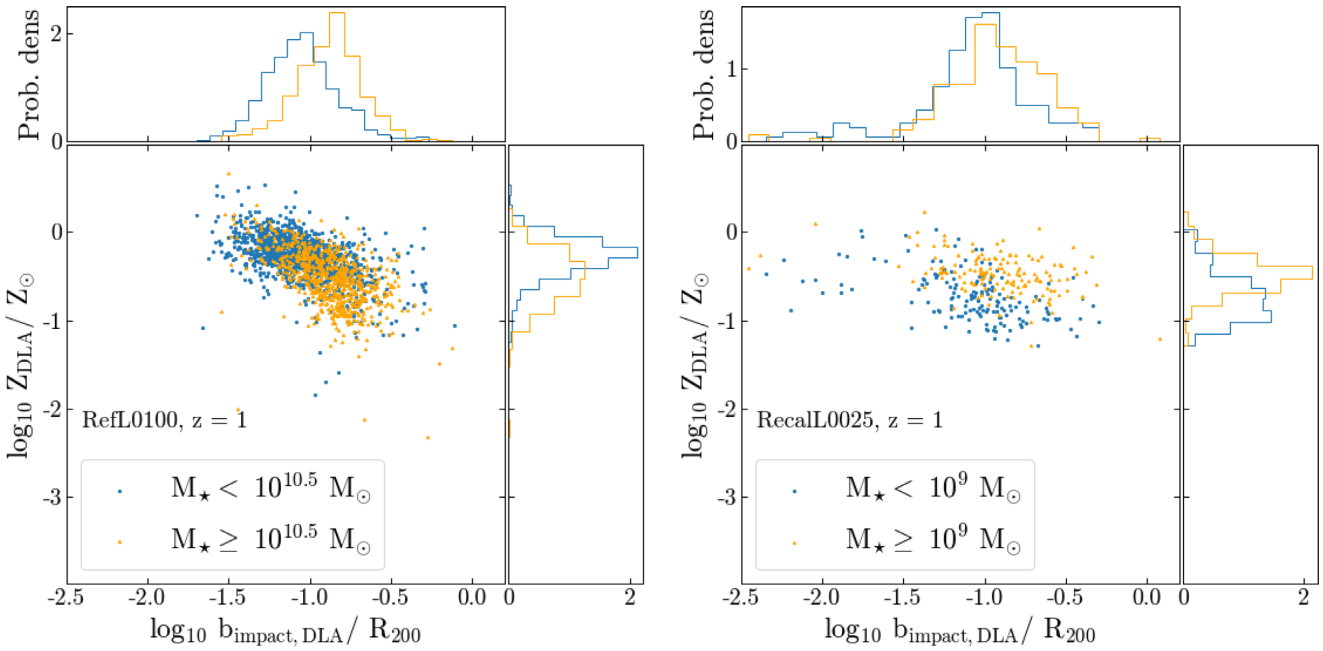


Figure 12. Main panels: the mean DLA metallicity ($Z_{\rm DLA}/Z_{\odot}$) versus the mean impact parameter, normalized by $R_{\rm 200c}$ (both calculated using 3D cells, see Section 2.3.3) for galaxies in the RefL0100 (left column) and RecalL0025 (right column) $z = 1$ samples, split into two stellar mass bins. Upper sub-panels: probability density distribution of $b_{\rm impact}/R_{\rm 200c}$ values of the galaxies in two different stellar mass bins. Right sub-panels: probability density distribution of $Z_{\rm DLA}/Z_{\odot}$ values of the galaxies in two different stellar mass bins.

mechanism of H I is smooth accretion, or diffuse accretion of the ionized IGM (Bauermeister, Blitz & Ma 2010), rather than the accretion of metal-rich material from stripped satellite galaxies. This was also found using EAGLE galaxies in Crain et al. (2017), where the authors compare the accretion rates of H I via smooth accretion and mergers, finding the former to dominate over our redshift range of interest ($z < 1$). Additionally, Wright et al. (2020) find that gas accretion (all gas, not just H I) comes mostly from smooth accretion of pristine gas across halo mass bins ranging from 10^9 to 10^{13} $M_{\odot}$ at $z = 1.1$ (at the 60 per cent level – see fig. 6 of Wright et al. 2020).

In order to further investigate the trends in DLA metallicity seen in fig. 11, we now plot the mean impact parameter of the DLA cells in each galaxy (again using the 3D grid which was used to calculate $f_{\rm vol}$) as a function of $Z_{{\rm vol},R_{200}}$ in Fig. 12 at $z = 1$. Here, we also show probability density distributions of the mean impact parameters and metallicities of the galaxies in our samples. The increase of normalized impact parameter with stellar mass is evident, particularly for the RefL0100 run. On the other hand, the two samples show differing trends in metallicity and stellar mass – the RecalL0025 run shows an increase in $Z_{{\rm vol},R_{200}}$ between the higher and lower stellar-mass bins ($<10^9$ and $\geq 10^9$ $M_{\odot}$, respectively), while the lower resolution, larger RefL0100 simulation shows a reduction in the peak of the metallicity distribution with stellar mass (between stellar mass bins $<10^{10.5}$ and $\geq 10^{10.5}$ $M_{\odot}$). The same trends are more pronounced at $z = 0$ (we do not include this plot for brevity). All stellar mass bins and both simulations show a reduction in DLA metallicity with impact parameter, although this trend is more significant in the intermediate resolution, larger EAGLE box (RefL0100). However, we know from Fig. 5 that the metallicity of the total gas in the galaxy is not converged in the simulation at the 10 per cent level and hence it is unclear whether the differences in DLA properties between the simulations are driven by something physical or are numerical in origin.

Despite the positive trend between relative impact parameter and $M_{\star}$ seen at $z = 1$ (Fig. 12) in the reference simulation (and to a lesser degree in RecalL0025), we note that the 2D covering fraction ($f_{\rm cov}$, calculated using face-on galaxies) of galaxies instead shows a slight reduction with halo mass at $z = 1$ (top plot, Fig. 7). To investigate whether this is due to projection effects, we plotted the mean impact parameter as calculated using the 3D cells, $b_{\rm impact,\,3d}$, minus the 2D impact parameter, calculated using a face-on orientation of the galaxies, as a function of stellar mass (Fig. 13). Should this difference be large, this would imply significant projection effects. We can see the relative difference between the two values (normalized by $R_{\rm 200c}$) is small until $\sim 10^{10}$ $M_{\odot}$ at both redshifts. At higher stellar masses, there is a positive correlation between $M_{\star}$ and the relative difference between impact parameters, indicating projection effects are having more of an impact on the observed properties of DLAs in massive galaxies. However, the extent of this impact appears to be resolution dependent, as RefL0100 and RecalL0025 are offset from each other (RecalL0025 shows a sharper upturn).

In order to investigate how the H I morphology, along with its kinematics, varies above and below the turnover stellar mass ($10^{10.5}$ $M_{\odot}$ at $z = 1$ and $z = 0$ in the RefL0100 EAGLE simulation), we plotted the probability distribution of $\kappa_{\rm H\,I}$ (the H I rotation parameter) for galaxies in two stellar mass bins: those with $M_{\star} < 10^{10.5}$ $M_{\odot}$ and those with $M_{\star} > 10^{11}$ $M_{\odot}$ (Fig. 14). Galaxies in the lower stellar-mass bin have higher $\kappa_{\rm H\,I}$ values, with the mean located above 0.67 at $z = 0$ and 0.6 at $z = 1$, our boundary between a disc/dispersion-dominated morphology (see Section 2.3.2). On the other hand, the galaxies with $M_{\star} > 10^{11}$ $M_{\odot}$ show lower $\kappa_{\rm H\,I}$ values, indicative of a more irregular H I morphology. This disparity in $\kappa_{\rm H\,I}$ is accentuated at $z = 0$. Therefore, Fig. 14 also supports the hypothesis that galaxies with larger stellar masses show a more irregular, dispersion-dominated H I distribution, with DLAs at higher impact parameters relative to $R_{\rm 200c}$.

Downloaded from https://academic.oup.com/mnras/article/501/3/4396/6041704 by Bodleian Library of the University of Oxford user on 01 April 2021

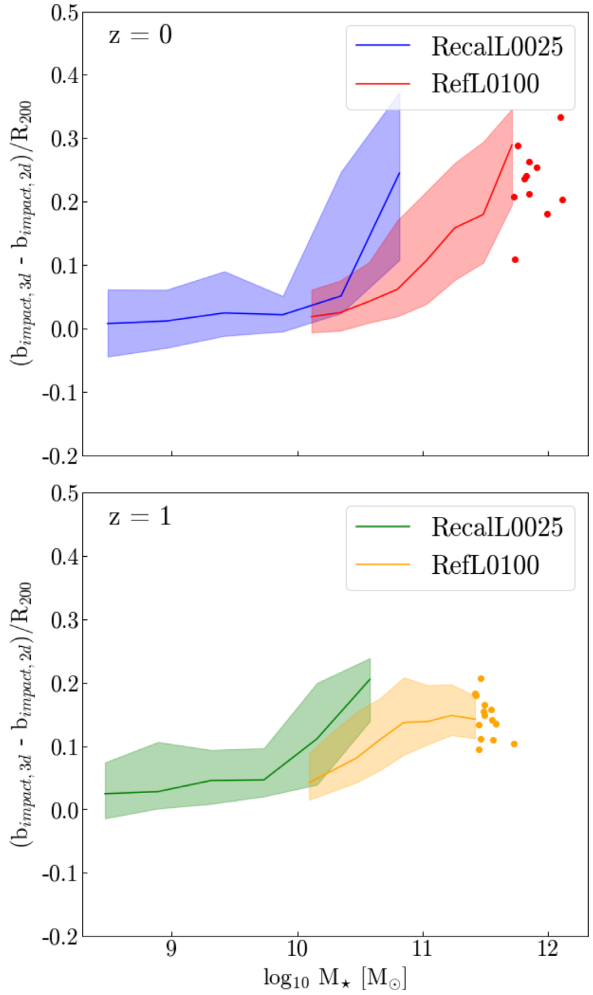


Figure 13. The difference between the impact parameters calculated using 3D cells ($b_{\rm impact,\,3d}$) and a 2D face-on projection of the galaxy ($b_{\rm impact,\,2d}$), normalized by $R_{\rm 200c}$, as a function of $M_\star$ at $z = 0$ (upper plot) and $z = 1$ (lower plot) for the RefL0100 (red, orange) and RecalL0025 (blue, green) EAGLE simulations. The solid lines are the median values for both simulations, while the shaded areas indicate the 16th–84th percentiles. Where there were fewer than 10 galaxies per stellar mass bin, the individual galaxies were plotted as points.

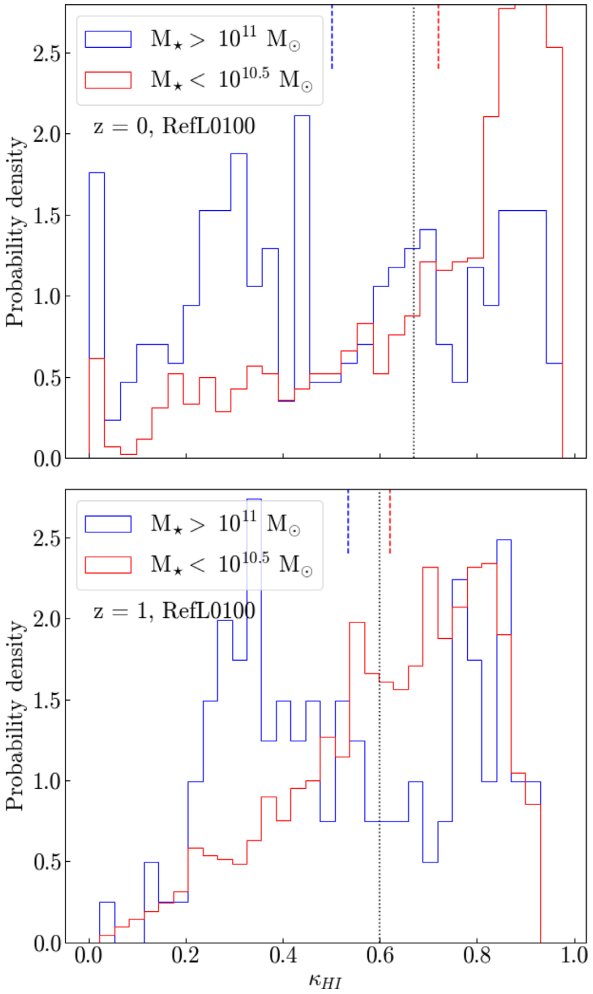


Figure 14. The normalized probability distributions of the H I rotation parameters, $\kappa_{\rm H\,I}$, of galaxies in two stellar mass bins – $>10^{11}$ M$_\odot$ (blue) and $<10^{10.5}$ M$_\odot$ (red) – for the RefL0100 EAGLE simulations at $z = 0$ (upper plot) and $z = 1$ (lower plot). The vertical dotted line indicates the values of $\kappa_{\rm H\,I}$ above which we consider the H I in a galaxy to be rotation dominated (this is redshift dependent).

3.4 Relative contribution of the CGM/ISM

In Section 3.1, we saw a significant mass of H I is around the galactic disc, most likely in the CGM. It is interesting to explore whether or not this translates into a population of CGM DLAs that are likely to be picked up by absorption surveys such as FLASH. We investigate the relative contribution of the CGM to the covering fraction of DLAs, and how this varies with both galaxy properties and redshift. We followed the method described in Section 2.4 in order to split our DLA grid cells into either ISM or CGM.

Initially, we focus on the global H I budget in our sample of galaxies and how the relative contribution of the CGM and ISM varies with redshift. The upper plot of Fig. 15 shows the H I-mass-weighted histogram of the ratio of the H I mass in the CGM compared with the total H I mass in both the ISM and the CGM ($f_{\rm cgm,H\,I}$). We can see the H I mass in the ISM dominates over the CGM inside galaxies in our sample at all redshift studied; the H I -mass-weighted mean $f_{\rm cgm,H\,I}$ value is $\leq$0.37 in both simulation boxes between $z = 0-2$. However, the distribution of $f_{\rm cgm,H\,I}$ values varies significantly with redshift – with the mean of the distribution increasing from 0.11 to 0.15 between $z = 0-2$ in the RecalL0025 simulation. On the other hand, the RefL0100 shows an initial reduction in the mean between $z = 0$ and $z = 1$; at $z = 0$ the majority of systems have a very low value for $f_{\rm cgm,H\,I}$, however there also exists a population of high-H I mass systems with high $f_{\rm cgm,H\,I}$ values that account for a significant portion of the total H I mass budget in the galaxy sample and hence skew the mean towards higher $f_{\rm cgm,H\,I}$. On the other hand, although the median (non-H I -mass-weighted) $f_{\rm cgm,H\,I}$ value increases between $z = 0$ and $z = 1$, the same high H I mass/high $f_{\rm cgm,H\,I}$ population of galaxies does not exist at this redshift, hence the H I-mass-weighted mean actually decreases from 0.37 to 0.3 (before increasing to 0.35 at $z = 2$).

There is a clear difference in the distributions of the two EAGLE boxes in Fig. 15, with RefL0025 showing lower H I CGM mass fractions than RefL0100. While this is true at all redshifts, the disparity between the mean CGM H I mass fraction is greatest at $z = 0$. In order to ascertain whether or not this disparity arises due to the fact the two boxes are sampling galaxy populations with different halo/stellar masses, we investigate the dependence of $f_{\rm cgm,H\,I}$ on

Downloaded from https://academic.oup.com/mnras/article/501/3/4396/6041704 by Bodleian Library of the University of Oxford user on 01 April 2021

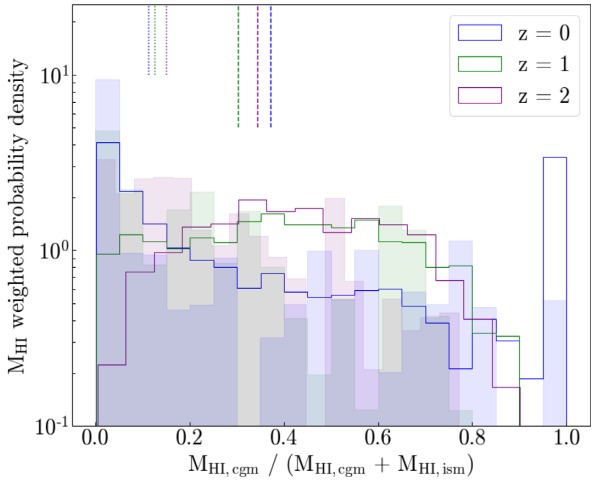


Figure 15. Probability density distribution of the ratio of the H I mass in the CGM compared with the total H I mass in both the ISM and the CGM ($f_{cgm,HI}$). The distributions are shown for redshift 0, 1, and 2 in blue, green, and purple, respectively. The filled histograms show the results from the RecalL0025 simulation, while the others are from the RefL0100 EAGLE box. The dashed vertical lines indicate the median of each RefL0100 distribution, while the shorter, dotted vertical lines indicate the median of the galaxies sampled from the RecalL0025 simulation.

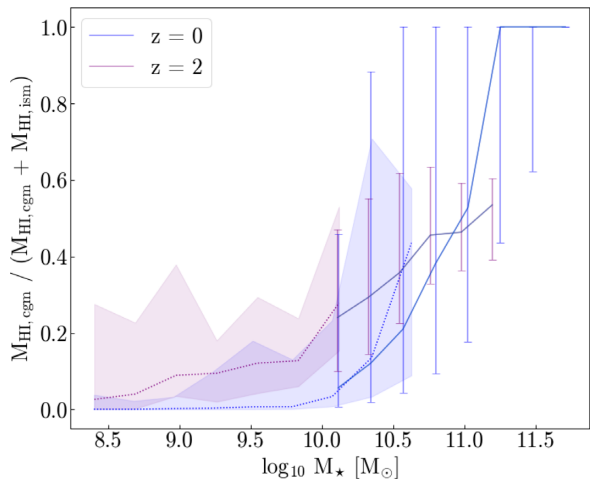


Figure 16. The median H I mass in the CGM compared with the total H I mass in both the ISM and the CGM ($Mf_{cgm,HI}$) in bins of stellar mass at redshifts 0 (blue) and 2 (purple) in the RecalL0025 (dashed lines) and RefL0100 (solid lines) EAGLE simulations. The solid vertical lines/shaded regions mark the 16th–84th percentiles of the RefL0100/RecalL0025 galaxy samples.

stellar mass in Fig. 16. Here, we only plot $z = 0$ and $z = 2$ for clarity. We can see that $f_{cgm,HI}$ increases with increasing stellar mass in all simulation boxes at both redshifts beyond 10^{10} $M_\odot$; however, the gradient is steeper at lower redshift. At $z = 0$, $f_{cgm,HI}$ is approximately 0 in all mass bins below 10^{10} $M_\odot$. By contrast, at $z = 2$ the H I CGM mass fraction increases gradually with stellar mass until 10^{10} $M_\odot$, when the gradient steepens significantly. Given the change in the $f_{cgm,HI}$–$M_\star$ relation occurs at 10^{10} $M_\odot$ (the location of the turnover in the GSMF) these results point to AGN feedback playing a role in the H I CGM mass fraction. This was also hinted at in Fig. 9, where a significant mass of H I was heated to higher temperatures (10^5 K) in higher mass galaxies.

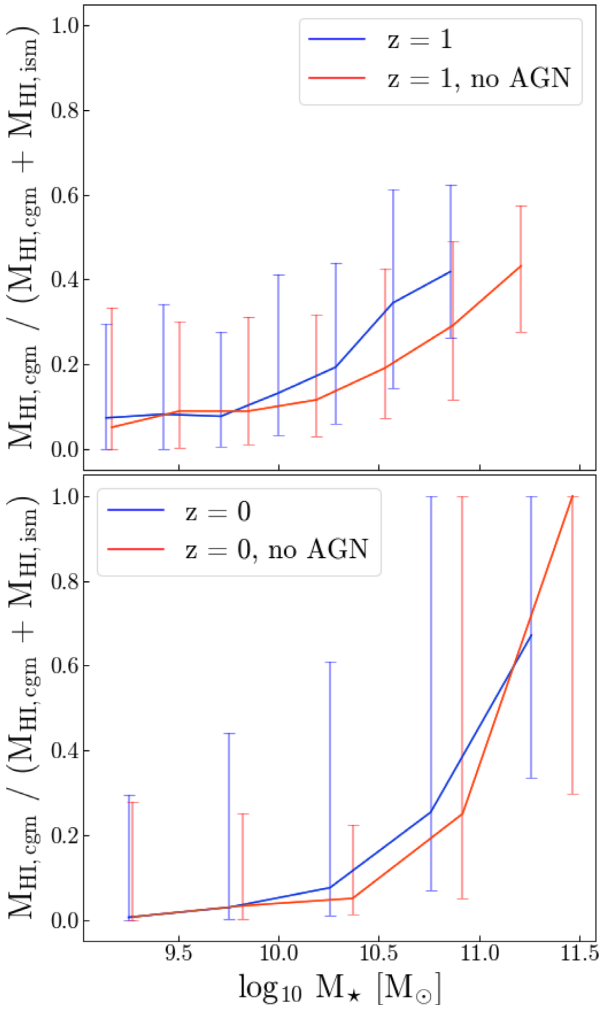


Figure 17. The median H I mass in the CGM compared with the total H I mass ($f_{cgm,HI}$) in stellar-mass bins at redshifts 1 (upper panel) and 0 (lower panel) in the RefL0050N0752 (blue lines) and NoAGNL0050N0752 (red lines) EAGLE simulations. The solid vertical lines mark the 16th–84th percentiles of the galaxy samples.

In order to investigate our hypothesis that the H I CGM mass fraction is intrinsically linked to AGN feedback, we re-plotted Fig. 16 at $z = 0$ and $z = 1$ for the RefL0050N0752 (blue) and NoAGNL0050N0752 (red) EAGLE simulations (Fig. 17). Focussing first at $z = 1$ (upper panel), the addition of AGN feedback acts to increase the median H I CGM mass relative to the total H I mass (CGM and ISM) for galaxies with stellar mass greater than $10^{9.75}$ $M_\odot$. Without AGN feedback, the $f_{cgm,HI}$–$M_\star$ relation also steepens for high stellar-mass galaxies; however, the gradient is shallower and begins to increase at a stellar mass ∼0.5 dex above that for the simulation that includes AGN feedback. Focussing instead at $z = 0$ (lower panel), the difference in the median $f_{cgm,HI}$ value in different stellar mass bins with/without AGN feedback is less pronounced. The principle effect of including AGN feedback is the significant increase in scatter in the $f_{cgm,HI}$–$M_\star$ relation towards higher $f_{cgm,HI}$ values, seen for galaxies with stellar masses below $10^{10.5}$ $M_\odot$. These results point to the importance of AGN feedback when considering the cold/cool phases of the CGM.

The offset in $f_{cgm,HI}$ value seen in Fig. 15 between simulations of different resolution is largely removed when accounting for stellar mass in Fig. 16, particularly at higher redshift. At $z = 0$, galaxies

Downloaded from https://academic.oup.com/mnras/article/501/3/4396/6041704 by Bodleian Library of the University of Oxford user on 01 April 2021

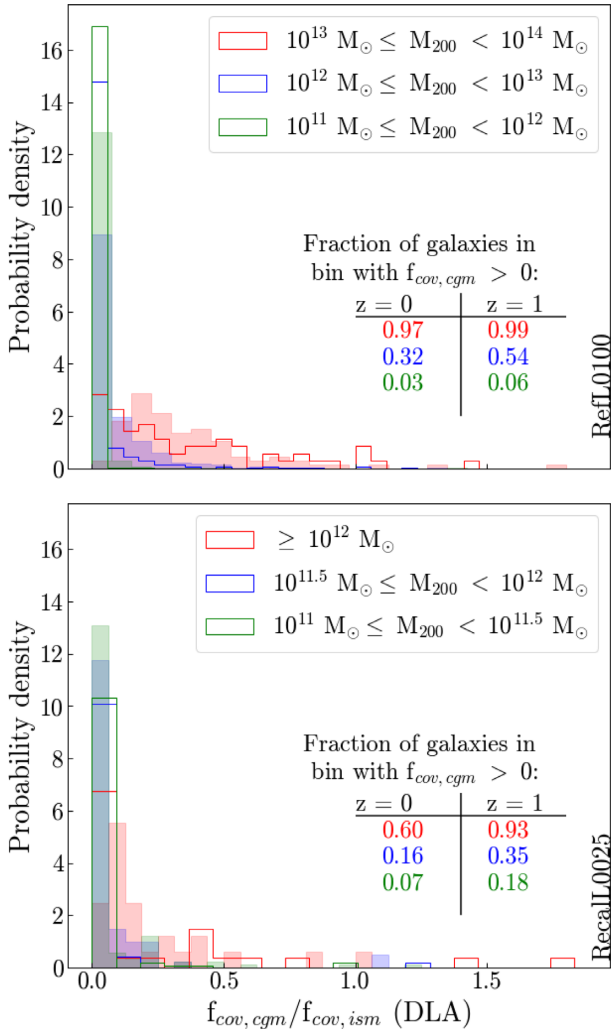


Figure 18. Normalized probability density distributions of the ratio $f_{\rm cov,\,cgm}/f_{\rm cov,\,ism}$ in M_{200} bins at $z = 0$ (non-filled histograms) and $z = 1$ (shaded histograms) in the RefL0100 EAGLE simulation (upper plot) and the RecalL0025 (lower plot). Here, we only plot galaxies with non-zero CGM covering fractions, while the fraction of the total number of galaxies in each mass range with a non-zero CGM fraction is listed on each plot.

in the RecalL0025 EAGLE box with stellar mass $>10^{10}$ M$_\odot$ have a median H I CGM fraction that is greater than galaxies in the intermediate resolution RefL0100 EAGLE box. This could either be due to the different feedback efficiencies adopted, in particular for the AGN feedback, or the change in numerical resolution. For example, van de Voort et al. (2019) argue that increasing the numerical resolution of the simulation results in a higher H I mass inside the CGM.

Therefore, given that the CGM contains a significant portion of the H I mass budget inside higher mass haloes, we might expect the covering fraction of CGM DLAs to be enhanced with respect to the ISM covering fraction in these galaxies. We investigate this in Fig. 18, which shows the probability density distributions of the fraction $f_{\rm cov,\,cgm}/f_{\rm cov,\,ism}$ at $z = 1$ and $z = 0$, using three different M_{200} bins (see Fig. 18) in both simulations (RefL0100 and RecalL0025). We do indeed see a shift towards higher values of the CGM/ ISM covering fraction ratio with increased stellar mass. This is present at both redshifts, but is more pronounced at $z = 1$. This is despite the fact we saw in Fig. 16 that the gradient in the $M_{\rm H\,I,cgm}$–$M_\star$ relation is shallower at higher redshift. In addition, the fraction of galaxies with a non-zero DLA-CGM covering fraction increases with redshift. As expected from Fig. 16, the fraction of galaxies with non-zero CGM covering fractions is significantly reduced in the RecalL0025 simulation compared with the RefL0100 sample, primarily due to the fact the simulation boxes are sampling different mass haloes/galaxies.

Our results indicate that the CGM plays an important role when considering the properties of DLAs in galaxies with high stellar/halo mass. Furthermore, the contribution of these higher impact parameter, lower metallicity CGM DLAs to blind H I observation surveys such as FLASH is likely to be enhanced at higher redshift. The mass and state of the H I in the CGM are subject to the detailed modelling of feedback physics, in particular AGN feedback. In this way, DLAs offer a way of further understanding and placing constraints on galactic feedback models.

3.5 The cold neutral medium

It is important to note that since 21-cm absorption surveys are sensitive to DLAs with the highest CNM fraction, it is unclear how many of CGM DLAs presented in Section 3.4 would be detected in a blind H I absorption survey such as FLASH. Moreover, our models assume either a two-phase (WNM and CNM) medium or hydrostatic equilibrium (see Section 2.3.1 for details), neither of which may apply in the CGM. In our follow-up paper, we will discuss the detailed properties and modelling of CGM DLAs, but this is beyond the scope of this paper. We investigate the redshift evolution of the CNM number densities (calculated using the outlined assumptions) for both the DLAs in the ISM and CGM in Fig. 19.

Fig. 19 shows there is an increase in the peak of the $n_{\rm CNM}$ probability distribution with redshift, visible for both ISM and CGM DLA. This hints that the CGM DLAs are more likely to be detected in 21-cm absorption surveys at higher redshift. The ISM DLAs show a high CNM density tail that is not present for the CGM DLAs, shifting the mean $n_{\rm CNM}$ towards higher values. However, the median $n_{\rm CNM}$ for the CGM DLAs is larger than that of the ISM at all redshift. This likely arises from the fact that the ISM has a higher metallicity than the CGM, along with a greater UV flux from SF regions, which shifts the molecular mass fraction towards a higher value for a given CNM fraction according to our model (see Section 2.3.1), reducing the assumed H I mass fraction accordingly.

3.6 Comparing $f_{\rm cov,R_{200}}$, $f_{\rm cov,\,70\,kpc}$, $f_{\rm vol,R_{200}}$

In order to explore any differences in the trends seen for $f_{\rm cov,R_{200}}$ and $f_{\rm vol,R_{200}}$ (in other words between the 2D covering fraction and the volume filling fraction) with galaxy properties, we re-plotted Fig. 7, using $f_{\rm vol,R_{200}}$ instead. We found no significant changes between the trends with sSFR and $\kappa_\star$. Fig. 20 shows the $f_{\rm vol,R_{200}}$–M_{200} relation. Here, we see the same turnover seen in Fig. 7 with stellar mass at $z = 0$. However, at $z = 1$ the $f_{\rm vol,R_{200}}$ declines across all halo masses, despite relatively constant $f_{\rm cov,R_{200}}$ values seen at $z = 1$ in Fig. 7 across a wide range of halo masses.

We hypothesize that the drop in $f_{\rm vol,R_{200}}$ with halo mass seen at $z = 1$, despite constant $f_{\rm cov,R_{200}}$ values, is caused by an increase in the clumpiness of DLAs with halo mass and a corresponding drop in the number of cells containing DLAs per sightline. This would result in a drop in $f_{\rm vol,R_{200}}$, despite a constant $f_{\rm cov,R_{200}}$ value. We explore this hypothesis in Figs 21 and 22. In Fig. 21, we show the H I-mass-weighted mean density of the gas in each galaxy against M_{200}. There is a positive correlation between ρ and M_{200} at $z = 0$ and

Downloaded from https://academic.oup.com/mnras/article/501/3/4396/6041704 by Bodleian Library of the University of Oxford user on 01 April 2021

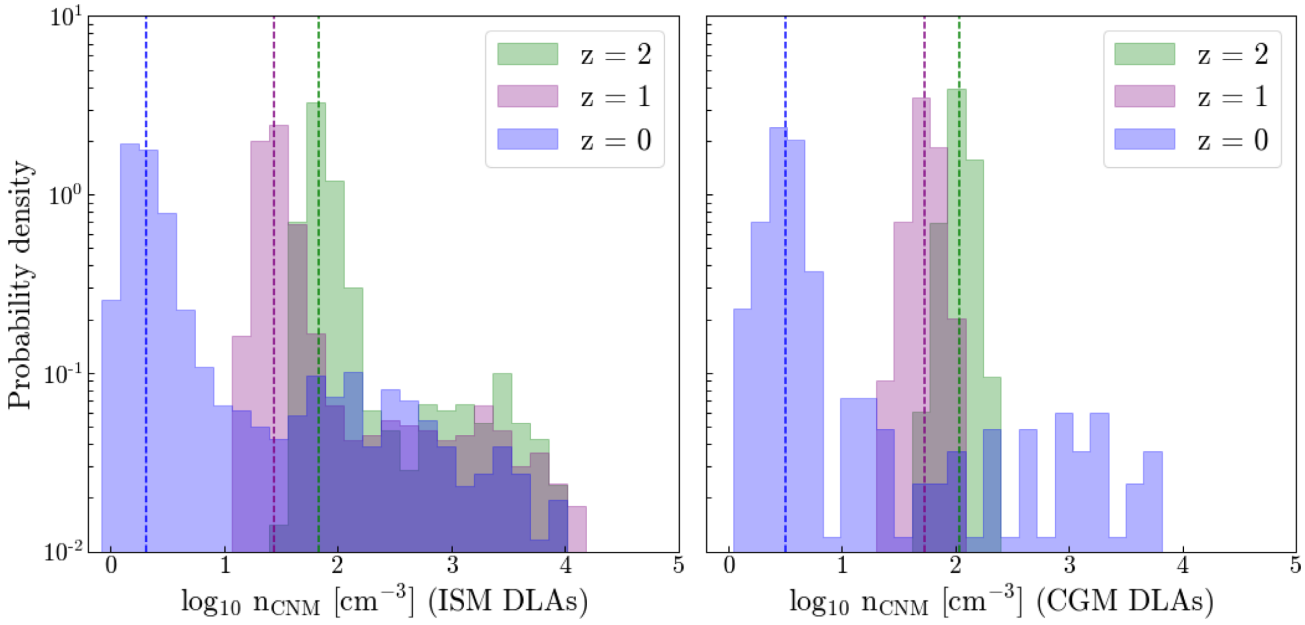


Figure 19. Normalized probability density distributions of the mean $n_{\rm CNM}$ calculated using our H I model (see Section 2.3.1) for DLAs in the ISM (left plot) and CGM (right plot) for galaxies in the RefL0100 EAGLE simulation as a function of redshift ($z = 0$ – blue, $z = 1$ – purple, $z = 0$ – green). The medians of each distribution are indicated using the dashed lines, coloured according to redshift.

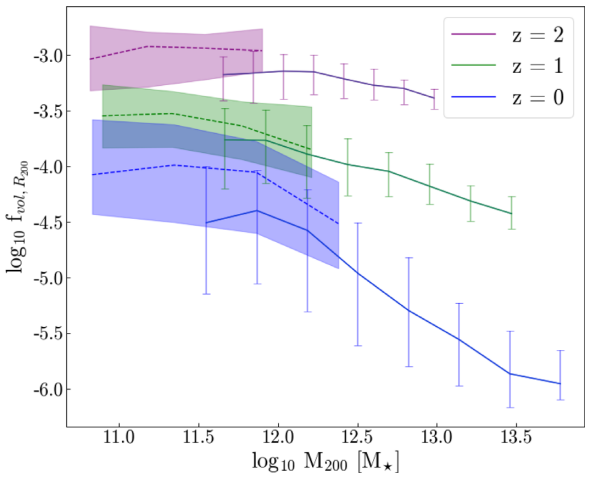


Figure 20. Figure to show the variation of $f_{{\rm vol},R_{200}}$ with M_{200} for our sample of galaxies taken from the RefL0100 (RecalL0025) EAGLE simulation at $z = 0$ (blue), $z = 0.5$ (green), and $z = 1$ (purple), with the median values shown as solid (dashed) lines and the 16th–84th percentile range shown using the capped vertical lines (shaded regions).

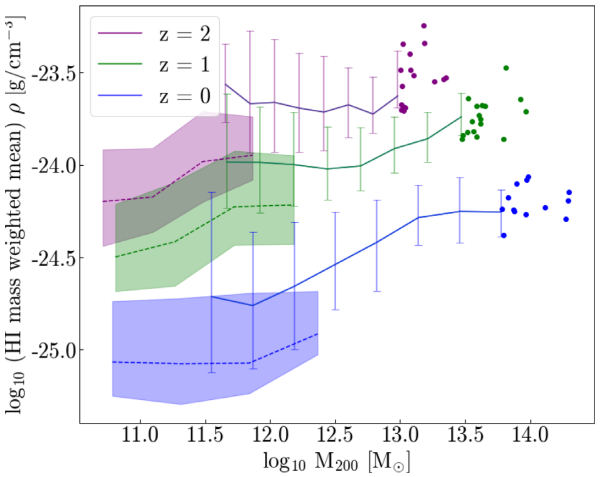


Figure 21. The mean H I mass-weighted density of the gas inside galaxies a function of M_{200} at $z = 0$ (blue), $z = 1$ (green), and $z = 2$ (purple). The solid/dashed lines indicate the median values for the galaxy sample taken from the RefL0100/RecalL0025 simulations, respectively. The 16th–84th percentile ranges are shown using the capped vertical lines/shaded areas for the RefL0100/ RecalL0025 simulations.

$z = 1$; however, a plateau/slight anticorrelation is seen at $z = 2$ in the RefL0100 EAGLE simulation. This shows that H I is on average denser in larger galaxies at $z \leq 1$, supporting the idea that DLAs are clumpier in these higher mass systems. It is also evident from Fig. 21 that the mean H I-mass-weighted density is systematically reduced in the higher resolution simulations. Since cooling is intrinsically linked to the metallicity of the gas (e.g. Wiersma et al. 2009b), and this is systematically lower in the higher resolution EAGLE box compared with the reference run, it follows that we would expect the mean density of the cool gas in RecalL0025 to be reduced compared with RefL0100 – if the gas is unable to cool as efficiently, it will be more resistant to fragmentation and collapse.

Fig. 22 shows the mean number of DLA-containing cells per sightline (defined as the 2D grid cells used when calculating $f_{\rm cov}$; referred to as $N_{\rm los}$ hereafter) against M_{200}. We also see a large scatter at halo masses $\lesssim 10^{12.25}\,{\rm M}_\odot$ (particularly at high redshift). However, beyond $\sim 10^{12.25}\,{\rm M}_\odot$ there is a negative trend between the two quantities at $z = 1$ – showing that the higher mass galaxies, on average, contain fewer DLA cells per individual sightline, which would result in a lower $f_{\rm vol}$ fraction, despite having a similar $f_{\rm cov}$ value to their lower mass counterparts. This trend extends to halo masses of $10^{12}\,{\rm M}_\odot$ at $z = 2$ and is also steeper at this redshift. The median $N_{\rm los}$ for galaxies at $z = 0$ is 1 across all halo masses in the RefL0100 EAGLE simulation; however, the higher resolution box shows an

Downloaded from https://academic.oup.com/mnras/article/501/3/4396/6041704 by Bodleian Library of the University of Oxford user on 01 April 2021

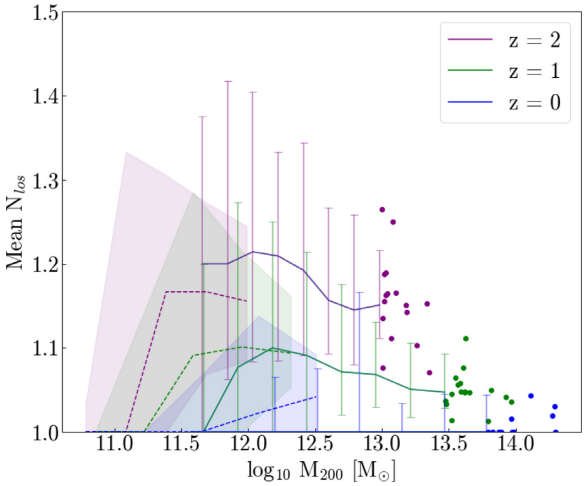


Figure 22. The number of DLA-containing cells that are summed over when calculating the column density of each pixel using the 2D face-on grid of each galaxy at $z = 0$ (blue), $z = 1$ (green), and $z = 2$ (purple). This is a proxy for the number of DLAs per sightline. The solid/dashed lines indicate the median values for the galaxy sample taken from the RefL0100/RecalL0025 simulations, respectively. The 16th–84th percentile ranges are shown using the capped vertical lines/shaded areas for the RefL0100/RecalL0025 simulations.

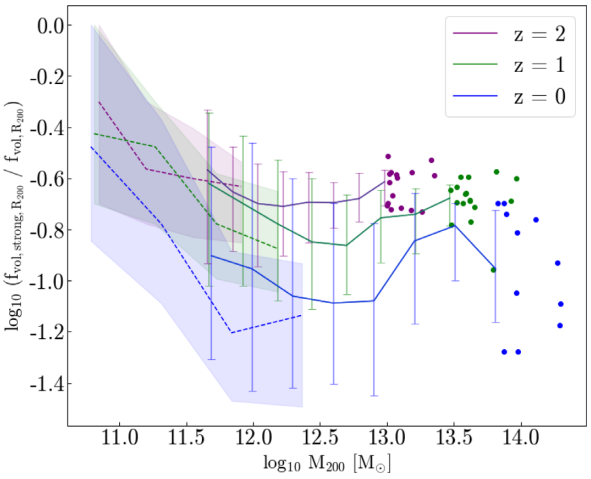


Figure 23. The ratio of the strong DLA volume-filling fraction to the total DLA volume fraction and how this changes with M_{200} at $z = 1$. Here, a DLA is characterized as 'strong' if its H I column density is greater than 10^{21} cm^{-2}. The median values in halo mass bins are indicated by the solid/dashed lines for the RefL0100/ RecalL0025 sample of galaxies. The 16th–84th percentile is range shown using the capped vertical lines/shaded regions for the RefL0100 EAGLE box/ the RecalL0025 run.

increase with halo mass at around 10^{12} $M_\odot$. These results support our hypothesis that at $z = 1$, the DLAs in both low- and high-mass galaxies inside our sample are clumpier, or less spatially extended, than those in haloes of intermediate halo masses ($\sim 10^{12.5}$ $M_\odot$).

We also investigate the ratio between the volume-filling fraction of strong DLAs (those with $N_{HI} > 10^{21}$ cm^{-2}) and all DLAs and how this varies with M_{200} in Fig. 23. This shows the opposite trends of Fig. 22, with an initial negative correlation between the two quantities until the turning point at $M_{200} \sim 10^{12}$–$10^{12.5}$ $M_\odot$ (depending on redshift), when the ratio starts to increase with halo mass. This indicates the relative contribution of strong DLAs to the $f_{vol,R_{200}}$ values increases with M_{200}, which is in agreement with the idea that the DLAs are denser and clumpier in these systems, reducing $f_{vol,R_{200}}$, despite a corresponding increase in the global H I mass (see Fig. 4) and a constant value of $f_{cov,R_{200}}$.

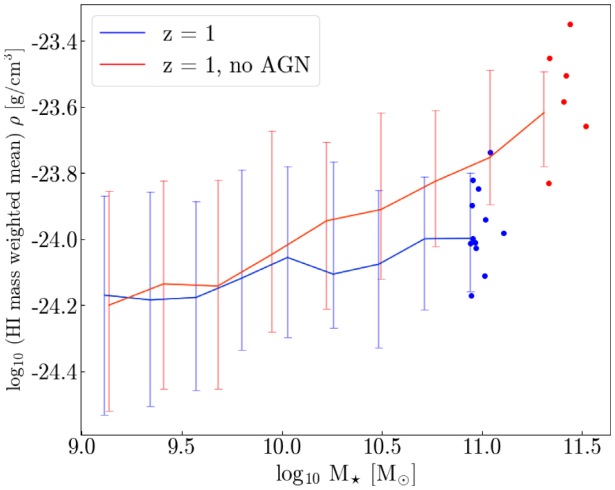


Figure 24. The mean H I-mass-weighted density of galactic gas as a function of stellar mass, using galaxies taken from the RefL0050N0752 (blue) and NoAGNL0050N0752 (red) EAGLE simulations at $z = 1$. The solid lines show the median values in 10 stellar mass bins, while the vertical lines indicate the 16th–84th percentile range. Points are plotted for individual galaxies where the stellar mass bin contains fewer than 10 galaxies.

In Fig. 24, we investigate whether or not the positive trend between halo mass and the H I-mass-weighted density, seen in Fig. 21, is impacted by AGN feedback. Here, we plot the mean H I-mass-weighted density of the gas in galaxies at $z = 1$, taken from the RefL0050N0752 (blue) and NoAGNL0050N0752 (red) EAGLE simulations, respectively. The addition of AGN feedback lowers the mean H I-mass-weighted density in galaxies with stellar masses above 10^{10} $M_\odot$. This result is complimentary to Fig. 17; the fact the CGM H I mass fraction of high-stellar-mass galaxies increases when AGN feedback is included implies a corresponding reduction in the mean H I-mass-weighted density of the gas in these galaxies. Moreover, we also see the drop in the mean H I-mass-weighted density is accompanied by a reduction in the volume-filling fraction of strong DLAs when AGN feedback is included (see Fig. 25). These results support our conclusion that AGN feedback impacts the physical properties of DLAs in high-mass galaxies. They are also consistent with work by Wright et al. 2020, who use EAGLE simulations to show the addition of AGN feedback produces galaxies with lower baryon fractions and baryonic accretion rates. This helps to explain why the volume-filling fraction of strong DLAs increases in the case when AGN feedback is not included – there is simply more cold, dense gas present in galaxies. Consequently, the AGN feedback model employed by cosmological simulations is likely an important factor when comparing the DLAs in simulated galaxies to those observed by surveys such as FLASH.

We also re-plotted Fig. 7 using $f_{cov,\,70\,kpc}$ instead (see Fig. 26). The trends in Fig. 26 are broadly consistent with those in Fig. 7; a turnover is still seen at $z = 0$ at $M_{200} \sim 10^{12}$ $M_\odot$, while at higher resolution there is a plateau in the covering fractions beyond 10^{12} $M_\odot$. There is also a marginally steeper gradient in the $f_{cov,\,70\,kpc}$–M_{200} at halo masses below 10^{12} $M_\odot$, compared with the gradient seen using the virial radius as the aperture in Fig. 7. This is driven by the use of a fixed aperture across a range of halo masses, while the H I disc extent

Downloaded from https://academic.oup.com/mnras/article/501/3/4396/6041704 by Bodleian Library of the University of Oxford user on 01 April 2021

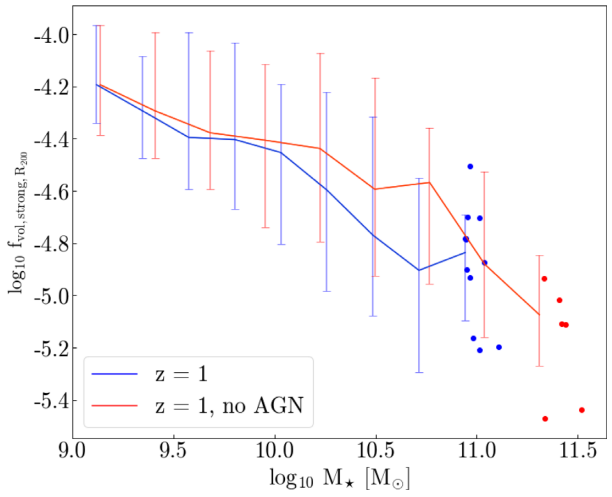


Figure 25. The volume-filling fraction (measured using an aperture of R_{200c}) of strong DLAs (defined as those with H I column densities greater than 10^{21} cm^{-2}) as a function of stellar mass, plotted using galaxies taken from the RefL0050N0752 (blue) and NoAGNL0050N0752 (red) EAGLE simulations at $z = 1$. The solid lines show the median values in 10 stellar mass bins, while the vertical lines indicate the 16th–84th percentile range. Points are plotted for individual galaxies where the stellar mass bin contains fewer than 10 galaxies.

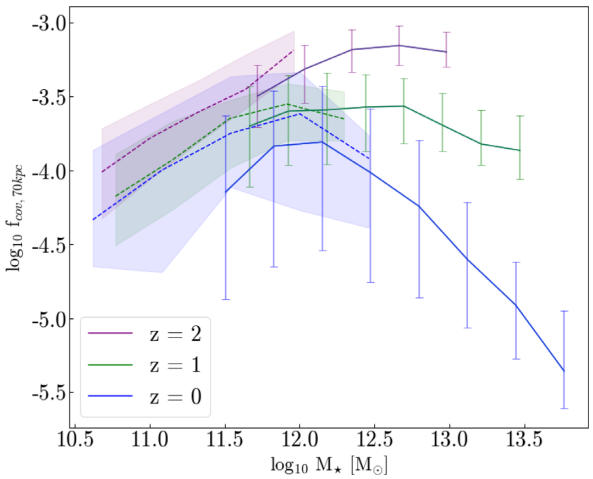


Figure 26. $f_{\rm cov,\,70\,kpc}$ as a function of M_{200} for our sample of galaxies taken from the RefL0100 (RecalL0025) EAGLE simulation at $z = 0$ (blue), $z = 1$ (green), and $z = 1$ (purple), with the median values shown as solid (dashed) lines and the 16th–84th percentile range shown using the capped vertical lines (shaded regions).

increases with halo mass. However, the presence of the peak in the $z = 0$ $f_{\rm cov,\,70\,kpc}$–M_{200} relation is likely due to a significant number of the DLAs in the higher mass systems being at radii larger than 70 kpc in the CGM of the halo, in agreement with the significant total H I mass outside 70 kpc seen in Fig. 4. This result is linked to the increase in impact parameter relative to R_{200c} at higher halo masses at $z = 0$ seen previously in Fig. 12.

4 DISCUSSION AND CONCLUSIONS

This paper set out to investigate the distribution and properties of DLAs in the EAGLE cosmological hydrodynamical simulations, focussing on the redshift range 0–2 in order to connect with the results from the next generation of 21-cm absorption surveys. The results of this paper can be summarized as follows:

(i) The H I-to-stellar mass ratio increases with redshift in EAGLE galaxies, with the most significant increase seen at $M_\star > 10^{10}$ M$_\odot$ (see Fig. 4). The H I masses obtained for the lower resolution, larger EAGLE box are systematically lower than those obtained at the same stellar mass in the high-resolution box. This is due to the higher gas metallicities of the former compared to the latter at fixed stellar mass, which leads to more efficient H_2 formation. This effect is lessened at higher redshift due to the central parts of galaxies in the high- and low-resolution boxes having similar metallicities, despite the average metallicity of gas in the galaxies being significantly higher in the lower resolution EAGLE simulation (see Fig. 5). The exact shape and normalization of the $M_{\rm H\,I}$–$M_\star$ relation is impacted by the chosen aperture in which the H I content in galaxies of stellar masses $> 10^{10}$ M$_\odot$ is measured (see Fig. 4), indicating that a significant fraction of the H I mass is at larger radii in these galaxies. This effect is seen both at $z = 0$ and $z = 1$.

(ii) The median DLA covering fraction obtained using an aperture of R_{200c}, $f_{\rm cov,\,DLA}$, shows a non-linear dependence on halo mass at $z = 0$, with a maximum at $\sim 10^{12}$ M$_\odot$. This maximum corresponds to the break of the GSMF both observationally and theoretically and is typically attributed to AGN/stellar feedback becoming efficient/inefficient at higher stellar masses. On the other hand, at $z = 1$, $f_{{\rm cov},R_{200}}$ does not vary over a wide range of halo masses. Moreover, there is a global shift towards higher DLA covering fractions (both 2D and 3D volume filling fractions) between $z = 0$ and $z = 1$.

(iii) On further investigation, we found the addition of AGN feedback had the largest impact on the covering fraction of DLAs at $z = 0$ for host galaxies in the stellar mass range 10^{10} M$_\odot$ $< M_\star \leq 10^{11}$ M$_\odot$, where it acts to reduce the DLA covering fraction (Fig. 8).

(iv) Looking instead at the kinematics of the H I, we find that EAGLE galaxies that are rotation dominated have, on average, higher covering fractions, when compared with galaxies that are dispersion dominated, indicating that galaxies with the highest DLA covering fractions also have orderly rotating H I discs (Fig. 10). High-stellar-mass galaxies were also shown to have lower $\kappa_{\rm H\,I}$ values. In other words, the kinematics of the H I is more dispersion dominated in these galaxies. However, the difference between galaxies in different mass bins lessens with increasing redshift.

(v) In Section 3.3, we saw that DLAs in EAGLE galaxies with high stellar masses ($>10^{10.5}$ M$_\odot$) had the highest impact parameters relative to their virial radius (Fig. 12), along with lower metallicities on average than those found in galaxies with stellar masses $<10^{10.5}$ M$_\odot$. Furthermore, these trends were not visible in the higher resolution RecalL0025 box; the DLAs in lower mass galaxies ($<10^9$ M$_\odot$) instead had marginally higher metallicities than those in higher stellar-mass galaxies ($\geq 10^9$ M$_\odot$) on average. Overall, our results indicate that the DLAs in systems of differing stellar mass trace different galaxy evolutionary processes. However, it is unclear if the process driving the differences seen between the two EAGLE boxes is physical, or numerical in origin.

(vi) The ISM dominates the total H I mass budget compared to the CGM in the majority of galaxies in our samples (see Fig. 15). However, we do see a trend of increasing H I mass fraction in the CGM relative to the ISM with increasing redshift. Moreover, the CGM H I mass fraction increases sharply with stellar mass above $\sim 10^{10}$ M$_\odot$ at all redshifts studied here, although the trend is steeper at $z = 0$ (see Fig. 16). This trend is present in both the intermediate- and high-resolution EAGLE boxes. Since this sharp increase of CGM H I mass fraction again occurs at the peak in the GSMF, it

Downloaded from https://academic.oup.com/mnras/article/501/3/4396/6041704 by Bodleian Library of the University of Oxford user on 01 April 2021

is likely DLAs in the CGM offer a way of further understanding and placing constraints on galactic feedback models, in particular AGN (see also Chauhan et al. 2020, for similar conclusions using semi-analytical models of galaxy formation). Moreover, using simulations with/without AGN feedback included, we found that the presence of an AGN acts to increase the scatter in CGM H I mass fraction for galaxies with $M_\star < 10^{10.5}$ M$_\odot$ at $z = 0$, while also increasing the median H I CGM mass fraction for galaxies with $M_\star \gtrsim 10^{10}$ M$_\odot$ at $z = 1$ (Fig. 17). The increase in CGM H I mass fraction in higher stellar-mass galaxies manifests as a correlation between the ratio of the CGM-to-ISM covering fraction and M_{200} (see Fig. 18). Additionally, this ratio increases with redshift.

(vii) In Section 3.6, we showed that the H I-mass-weighted gas density increases with increasing halo mass (see Fig. 21). This is accompanied with a larger relative covering fraction of strong DLAs and fewer DLAs per sightline (Figs 23 and 22, respectively). This resulted in the $f_{\mathrm{vol},R_{200}}$ anticorrelating with halo mass at $z = 1$, despite a constant $f_{\mathrm{cov},R_{200}}$ across a range of halo masses (see Figs 7 and 20). A peak in the number of DLAs per sightline and a corresponding dip in the fraction of strong DLAs is seen at a halo mass between 10^{12}–$10^{12.5}$ M$_\odot$, depending on redshift. We investigated whether or not this could be impacted by the action of AGN feedback, finding that the addition of an AGN feedback model acts to reduce the mean H I -mass-weighted density in galaxies with stellar masses above 10^{10} M$_\odot$ at $z = 1$ (Fig. 24). There is also a corresponding reduction in the volume-filling fraction of strong DLAs in these high-stellar-mass galaxies.

(viii) In the appendices, we show that the effects of altering the H I–H$_2$ model are not significant compared with altering the resolution of the simulation and, in doing so, the distribution of metals in galaxies along with the feedback (AGN and stellar) models. It is therefore imperative to understand and constrain the effects of both AGN and stellar feedback, along with radial metallicity distribution, on the H I content of the CGM and ISM, in order to fully understand the results of the cosmological simulations with regard to DLAs.

4.1 Caveats

One of the key results of this paper is that the high-stellar-mass galaxies in our sample have clumpier, stronger DLAs, which have a higher mean relative impact parameter and lower metallicities. As discussed in Section 2.3.1, we know from Rahmati et al. (2013b) that the effects of LSR on strong DLAs are highly uncertain, hence this introduces a degree of uncertainty to these results. In future work, we would like to investigate the impact of LSR on these strong, clumpy DLAs. However, given the fraction of the DLAs in the CGM is higher in these galaxies, it is likely LSR will have a limited impact on the low metallicity, high impact parameter DLAs.

Furthermore, we have consistently seen that the metallicities of the DLAs in the higher resolution boxes are systematically lower than those in the lower resolution box, which in turn impacts the H I/H$_2$ fractions, along with cooling properties of the gas. We saw in Fig. 5 that the situation is actually better when we consider the radial metallicity dependence at $z = 1$. Yet, how this alteration in metallicity affects our results is not easy to decipher, since rapid cooling supports both the formation of higher density H I clumps *and* the removal of H I via the formation of H$_2$.

Both the H I/H$_2$ breakdown and the simulations themselves are based on a spatial resolution of the order of 1 kpc (the softening length for the RefL0100 run is 0.7 pkpc – see table 2 of Schaye et al. 2015), which is at least a factor of 10 greater than the average (giant) molecular cloud/molecular cloud width. Our results therefore average across a wider area, meaning we are missing the detailed kinematics/mixing of the two neutral gas phases. Therefore, our DLA properties should be seen as global averages across the whole galaxy.

4.2 Our results in context

We have shown that AGN feedback is linked to the volume-filling fraction of strong DLAs, along with the mean density of H I gas in high-stellar-mass galaxies. In this way, our results suggest that DLAs and their physical properties offer a potential tracer for AGN feedback and its impact on the host galaxy. This links to both ongoing work into the cold component of AGN outflows (e.g. Lehnert et al. 2011; Morganti et al. 2016), along with the complex interplay between AGN outflows and in-flowing gas (e.g. Riffel, Storchi-Bergmann & Riffel 2015). Our future work will focus on this and in particular how both AGN and stellar feedback impact not only the properties of DLAs, but also the fraction of these in the CGM.

This paper has focused on galaxies with stellar masses $>10^8$ M$_\odot$ due to resolution constraints. However, we know from plots such as Figs 23 and 12 that the DLAs associated with lower stellar-mass galaxies (those located to the left of the GSMF) and higher mass galaxies (those beyond the peak in the GSMF) likely differ in physical origins and follow opposing trends. Therefore, pushing towards the lower end of the GSMF would offer key insights into this transition seen in the DLA population. We know AGN feedback is intrinsically linked to the properties of DLAs in higher mass systems, hence it is likely that stellar feedback also greatly impacts the H I budget in smaller, dwarf galaxies. In order to delve more deeply into the relative impact of different types of stellar feedback on dwarf galaxies, and in particular how this changes the DLA abundance in the CGM, cosmological zoom-in simulations are needed (recent work on this includes Rhodin et al. 2018).

The role of the CGM in galaxy evolution has been an area of intense interest in recent years, with multiple papers linking an enhancement in numerical resolution of simulations to a boost in the column density of low ions such as H I inside the CGM (Hummels et al. 2019; van de Voort et al. 2019). Given our results point to a significant fraction of the DLAs in high-mass galaxies originating in the CGM, it would be of interest to study these systems using cosmological zoom-in simulations.

Recent results from the FLASH survey (Allison et al. 2020) indicate the presence of large quantities of H I at a high impact parameter ($\sim$17 kpc) in an intervening absorbing galaxy. Our results support the hypothesis that at high redshift, higher relative impact parameters are more likely for DLAs in galaxies of high stellar mass. Our results also indicate that the properties of detected DLAs are intrinsically linked with the host galaxy properties, such as mass and star formation rate. For example, DLAs in intermediate-mass galaxies ($M_\star \sim 10^{10}$ M$_\odot$) are more likely to trace recycled H I than those in lower and higher stellar-mass galaxies (see Fig. 11).

ACKNOWLEDGEMENTS

This research was supported by the Australian Research Council Centre of Excellence for All Sky Astrophysics in 3 Dimensions (ASTRO 3D), through project number CE170100013. JRA acknowledges support from a Christ Church Career Development Fellowship. ARHS acknowledges the receipt of the Jim Buckee Fellowship at ICRAR-UWA. This work was supported by resources provided by the Pawsey Supercomputing Centre with funding from the Australian Government and the Government of Western Australia. LGS thanks Benedikt Diemer for use of his UV propagation code, described in Section 2.3.1 of this paper. CL thanks the MERAC Foundation

Downloaded from https://academic.oup.com/mnras/article/501/3/4396/6041704 by Bodleian Library of the University of Oxford user on 01 April 2021

for a Postdoctoral Research Award. The Cosmic Dawn Center of Excellence is funded by the Danish National Research Foundation under the grant No. 140. We have used PYTHON for our data analysis and acknowledge the use of MATPLOTLIB (Hunter 2007) to generate the plots in this paper.

DATA AVAILABILITY

This paper uses the public data release of the EAGLE simulation suite (Crain et al. 2015; McAlpine et al. 2016; Schaye et al. 2015; The EAGLE team 2017) and the data underlying this article are available at http://icc.dur.ac.uk/Eagle/database.php. We also use the data from the extended GALEX Arecibo SDSS Survey (xGASS; Catinella et al. 2018) available at https://xgass.icrar.org/data.html, along with the publicly available photoionization tables given by Haardt & Madau (2012), available at: http://www.ucolick.org/~pmadau/CUBA/HOME.html.

REFERENCES

Allison J. R., Zwaan M. A., Duchesne S. W., Curran S. J., 2016, MNRAS, 462, 1341
Allison J. R. et al., 2020, MNRAS, 494, 3627
Altay G., Theuns T., Schaye J., Booth C. M., Dalla Vecchia C., 2013, MNRAS, 436, 2689
Bahé Y. M. et al., 2016, MNRAS, 456, 1115
Bauermeister A., Blitz L., Ma C.-P., 2010, ApJ, 717, 323
Beckmann R. S. et al., 2017, MNRAS, 472, 949
Berg T. A. M. et al., 2017, MNRAS, 464, L56
Berry M., Somerville R. S., Haas M. R., Gawiser E., Maller A., Popping G., Trager S. C., 2014, MNRAS, 441, 939
Berry M., Somerville R. S., Gawiser E., Maller A. H., Popping G., Trager S. C., 2016, MNRAS, 458, 531
Bird S., Vogelsberger M., Haehnelt M., Sijacki D., Genel S., Torrey P., Springel V., Hernquist L., 2014, MNRAS, 445, 2313
Bird S., Garnett R., Ho S., 2017, MNRAS, 466, 2111
Bower R. G., Schaye J., Frenk C. S., Theuns T., Schaller M., Crain R. A., McAlpine S., 2017, MNRAS, 465, 32
Catinella B. et al., 2018, MNRAS, 476, 875
Chauhan G., Lagos C. d. P., Stevens A. R. H., Obreschkow D., Power C., Meyer M., 2020, MNRAS, 498, 44
Chowdhury A., Kanekar N., Chengalur J. N., Sethi S., Dwarakanath K. S., 2020, Nature, 586, 369
Correa C. A., Schaye J., Clauwens B., Bower R. G., Crain R. A., Schaller M., Theuns T., Thob A. C. R., 2017, MNRAS, 472, L45
Cortese L., Catinella B., Boissier S., Boselli A., Heinis S., 2011, MNRAS, 415, 1797
Crain R. A. et al., 2015, MNRAS, 450, 1937
Crain R. A. et al., 2017, MNRAS, 464, 4204
Cullen L., Dehnen W., 2010, MNRAS, 408, 669
Dalla Vecchia C., Schaye J., 2012, MNRAS, 426, 140
Davé R., Katz N., Oppenheimer B. D., Kollmeier J. A., Weinberg D. H., 2013, MNRAS, 434, 2645
Davé R., Crain R. A., Stevens A. R. H., Narayanan D., Saintonge A., Catinella B., Cortese L., 2020, MNRAS, 497, 146
Davidzon I. et al., 2017, A&A, 605, A70
Davis M., Efstathiou G., Frenk C. S., White S. D. M., 1985, ApJ, 292, 371
Decarli R. et al., 2019, ApJ, 882, 138
Diemer B. et al., 2018, ApJS, 238, 33
Dolag K., Borgani S., Murante G., Springel V., 2009, MNRAS, 399, 497
Driver S. P. et al., 2018, MNRAS, 475, 2891
Durier F., Dalla Vecchia C., 2012, MNRAS, 419, 465
Fernández X. et al., 2016, ApJ, 824, L1
Fumagalli M., O'Meara J. M., Prochaska J. X., Rafelski M., Kanekar N., 2015, MNRAS, 446, 3178
Fynbo J. P. U. et al., 2011, MNRAS, 413, 2481
Gnedin N. Y., Kravtsov A. V., 2011, ApJ, 728, 88
Grasha K., Darling J., Leroy A. K., Bolatto A. D., 2020, MNRAS, 498, 883
Gupta N. et al., 2016, in Proc. MeerKAT Science: On the Pathway to the SKA. Stellenbosch, South Africa, p. 14
Haardt F., Madau P., 1996, ApJ, 461, 20
Haardt F., Madau P., 2001, in Neumann D. M., Tran J. T. V., eds, Clusters of Galaxies and the High Redshift Universe Observed in X-rays, XXIst Moriond Astrophysics Meeting. CEA, Savoie, p. 64
Haardt F., Madau P., 2012, ApJ, 746, 125
Hopkins P. F., 2013, MNRAS, 428, 2840
Hughes T. M., Cortese L., Boselli A., Gavazzi G., Davies J. I., 2013, A&A, 550, A115
Hummels C. B. et al., 2019, ApJ, 882, 156
Hunter J. D., 2007, Comput. Sci. Eng., 9, 90
Johnston S. et al., 2007, Publ. Astron. Soc. Aust., 24, 174
Kanekar N. et al., 2014, MNRAS, 438, 2131
Krogager J. K., Møller P., Fynbo J. P. U., Noterdaeme P., 2017, MNRAS, 469, 2959
Krumholz M. R., 2013, MNRAS, 436, 2747
Krumholz M. R., McKee C. F., 2005, ApJ, 630, 250
Krumholz M. R., McKee C. F., Tumlinson J., 2009, ApJ, 699, 850
Lagos C. d. P. et al., 2015, MNRAS, 452, 3815
Lagos C. d. P. et al., 2016, MNRAS, 459, 2632
Lehnert M. D., Tasse C., Nesvadba N. P. H., Best P. N., van Driel W., 2011, A&A, 532, L3
Leroy A. K., Walter F., Brinks E., Bigiel F., de Blok W. J. G., Madore B., Thornley M. D., 2008, AJ, 136, 2782
Liske J. et al., 2015, MNRAS, 452, 2087
Mackenzie R. et al., 2019, MNRAS, 487, 5070
Madau P., 1995, ApJ, 441, 18
Madau P., Dickinson M., 2014, ARA&A, 52, 415
Madau P., Haardt F., Rees M. J., 1999, ApJ, 514, 648
Marasco A., Crain R. A., Schaye J., Bahé Y. M., van der Hulst T., Theuns T., Bower R. G., 2016, MNRAS, 461, 2630
McAlpine S. et al., 2016, Astron. Comput., 15, 72
McKee C. F., Krumholz M. R., 2010, ApJ, 709, 308
Mitchell P. D. et al., 2018, MNRAS, 474, 492
Monier E. M., Turnshek D. A., Rao S. M., Sardane G. M., Burdette D., 2019, MNRAS, 483, 1168
Morganti R., Veilleux S., Oosterloo T., Teng S. H., Rupke D., 2016, A&A, 593, A30
Murray C. E., Stanimirović S., Goss W. M., Heiles C., Dickey J. M., Babler B., Kim C.-G., 2018, ApJS, 238, 14
Møller P., Warren S. J., 1998, MNRAS, 299, 661
Nagamine K., Springel V., Hernquist L., 2004, MNRAS, 348, 421
Neeleman M., Prochaska J. X., Ribaudo J., Lehner N., Howk J. C., Rafelski M., Kanekar N., 2016, ApJ, 818, 113
Noterdaeme P., Petitjean P., Ledoux C., Srianand R., 2009, A&A, 505, 1087
Noterdaeme P. et al., 2012, A&A, 547, L1
Ostriker E. C., McKee C. F., Leroy A. K., 2010, ApJ, 721, 975
Péroux C., Bouché N., Kulkarni V. P., York D. G., Vladilo G., 2011, MNRAS, 410, 2237
Price D. J., 2008, J. Comput. Phys., 227, 10040
Prochaska J. X., Wolfe A. M., 1997, ApJ, 487, 73
Prochaska J. X., Wolfe A. M., 2009, ApJ, 696, 1543
Prochaska J. X. et al., 2017, ApJ, 837, 169
Rafelski M., Neeleman M., Fumagalli M., Wolfe A. M., Prochaska J. X., 2014, ApJ, 782, L29
Rahmati A., Schaye J., 2014, MNRAS, 438, 529
Rahmati A., Pawlik A. H., Raičević M., Schaye J., 2013a, MNRAS, 430, 2427
Rahmati A., Schaye J., Pawlik A. H., Raičević M., 2013b, MNRAS, 431, 2261
Rahmati A., Schaye J., Bower R. G., Crain R. A., Furlong M., Schaller M., Theuns T., 2015, MNRAS, 452, 2034
Rahmani H. et al., 2016, MNRAS, 463, 980

Downloaded from https://academic.oup.com/mnras/article/501/3/4396/6041704 by Bodleian Library of the University of Oxford user on 01 April 2021

Rao S. M., Turnshek D. A., Sardane G. M., Monier E. M., 2017, MNRAS, 471, 3428
Rhee J., Lah P., Briggs F. H., Chengalur J. N., Colless M., Willner S. P., Ashby M. L. N., Le Fèvre O., 2018, MNRAS, 473, 1879
Rhodin N. H. P., Christensen L., Møller P., Zafar T., Fynbo J. P. U., 2018, A&A, 618, A129
Rhodin N. H. P., Agertz O., Christensen L., Renaud F., Fynbo J. P. U., 2019, MNRAS, 488, 3634
Riffel R. A., Storchi-Bergmann T., Riffel R., 2015, MNRAS, 451, 3587
Rosas-Guevara Y. M. et al., 2015, MNRAS, 454, 1038
Rubin K. H. R., Hennawi J. F., Prochaska J. X., Simcoe R. A., Myers A., Lau M. W., 2015, ApJ, 808, 38
Sadler E. M. et al., 2020, MNRAS, 499, 4293
Saintonge A. et al., 2016, MNRAS, 462, 1749
Sales L. V., Navarro J. F., Schaye J., Dalla Vecchia C., Springel V., Booth C. M., 2010, MNRAS, 409, 1541
Sánchez-Ramírez R. et al., 2016, MNRAS, 456, 4488
Schaye J., 2004, ApJ, 609, 667
Schaye J., Dalla Vecchia C., 2008, MNRAS, 383, 1210
Schaye J. et al., 2015, MNRAS, 446, 521
Springel V., 2005, MNRAS, 364, 1105
Springel V., White S. D. M., Tormen G., Kauffmann G., 2001, MNRAS, 328, 726
Stevens A. R. H. et al., 2019a, MNRAS, 483, 5334
Stevens A. R. H., Diemer B., Lagos C. d. P., Nelson D., Obreschkow D., Wang J., Marinacci F., 2019b, MNRAS, 490, 96
The EAGLE team, 2017, preprint(arXiv:1706.09899)
Thob A. C. R. et al., 2019, MNRAS, 485, 972
Tomczak A. R. et al., 2014, ApJ, 783, 85
Turnshek D. A., Rao S. M., Nestor D. B., Belfort-Mihalyi M., Quider A. M., 2005, in Williams P., Shu C.-G., Menard B., eds, Proceedings IAU Colloq. 199: Probing Galaxies through Quasar Absorption Lines. Cambridge Univ. Press 2005, Cambridge, p. 104
van de Voort F., Springel V., Mandelker N., van den Bosch F. C., Pakmor R., 2019, MNRAS, 482, L85
Wang J. et al., 2011, MNRAS, 412, 1081
Wang J. et al., 2017, MNRAS, 472, 3029
Wiersma R. P. C., Schaye J., Smith B. D., 2009a, MNRAS, 393, 99
Wiersma R. P. C., Schaye J., Theuns T., Dalla Vecchia C., Tornatore L., 2009b, MNRAS, 399, 574
Wolfe A. M., Gawiser E., Prochaska J. X., 2005, ARA&A, 43, 861
Wolfire M. G., McKee C. F., Hollenbach D., Tielens A. G. G. M., 2003, ApJ, 587, 278
Wright R. J., Lagos C. d. P., Power C., Mitchell P. D., 2020, MNRAS, 498, 1668
York D. G. et al., 2000, AJ, 120, 1579
Zhang W., Li C., Kauffmann G., Zou H., Catinella B., Shen S., Guo Q., Chang R., 2009, MNRAS, 397, 1243
Zhou Z., Wu H., Zhou X., Ma J., 2018, PASP, 130, 094101

APPENDIX A: DIFFERENT H I–H_2 DECOMPOSITION METHOD(S)

A1 Gnedin 2011 breakdown

Here, we compare the results of the Krumholz (2013) method (or K13) with an alternative method for calculating the ratio of molecular to neutral Hydrogen (f_{H_2}), which uses the fitting formulae described in Gnedin & Kravtsov (2011) to relate the dust-to-gas ratio and the interstellar far-UV (FUV) flux to the atomic-to-molecular transition in the ISM of the simulation. Gnedin & Kravtsov (2011) derived these fitting formulae using simulations of a snapshot of a cosmological simulation taken at $z = 4$ and evolved using 3D radiative transfer and an H/He chemical network, along with a H_2 formation model. We refer to this method as G11 in the text.

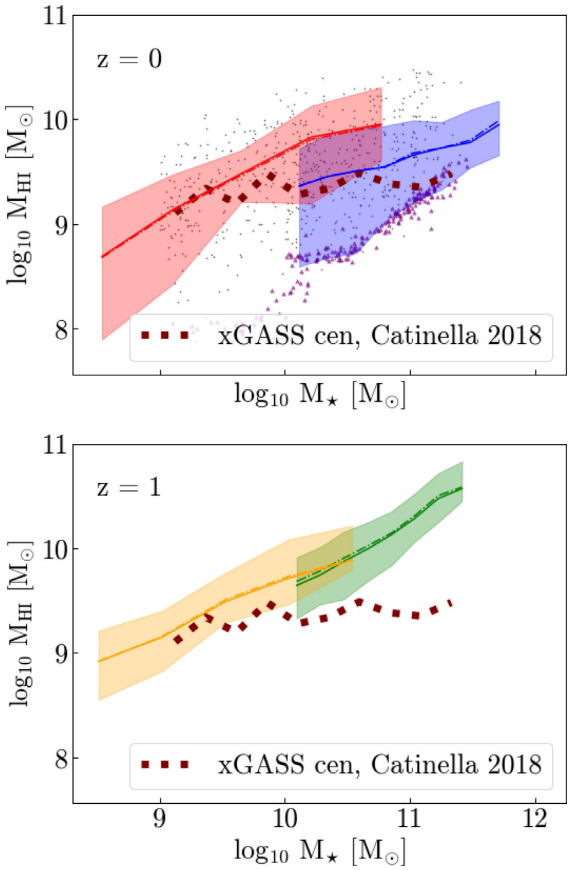


Figure A1. Plot of $M_{H\,I}$–$M_\star$ at $z = 0$ (top plot) and $z = 1$ (lower plot), as calculated for both EAGLE box RecalL0025 (red/orange, respectively) and RefL0100 (blue and green, respectively) using both the G11 H I–H_2 breakdown model (dot–dashed lines) and the K13 model (solid lines). The solid/dot–dashed lines indicate the median values in 10 stellar mass bins for each galaxy sample, while the shaded regions are the 16th–84th percentile range inside each stellar mass bin for the G11 model. Also plotted is a representative sample of the $M_{H\,I}$ and $M_\star$ values obtained by the xGASS survey (Catinella et al. 2018) (black dots/purple triangles for detections/non-detections) for central galaxies in the local Universe, along with the median values (dashed line).

Fundamentally, Gnedin & Kravtsov (2011) parametrize f_{H_2} (this has the same meaning as above) as

$$f_{H_2} \approx \frac{1}{1 + \exp(-4x - 3x^3)}, \tag{A1}$$

where x can be expressed as

$$x = \Lambda^{3/7} \ln\left(\frac{Zn_H}{Z_\odot \Lambda n_\star}\right), \tag{A2}$$

with $n_\star = 25\,\mathrm{cm}^{-3}$, while

$$\Lambda = \ln(1 + g(Z/Z_\odot)^{3/7}(G_0'/15)^{4/7}). \tag{A3}$$

Furthermore, the g factor is given by

$$g = \frac{1 + \alpha s + s^2}{1 + s}, \tag{A4}$$

with s, α, and $D_\star$ defined by

$$s = \frac{0.04}{D_\star + (Z/Z_\odot)}, \tag{A5}$$

Downloaded from https://academic.oup.com/mnras/article/501/3/4396/6041704 by Bodleian Library of the University of Oxford user on 01 April 2021

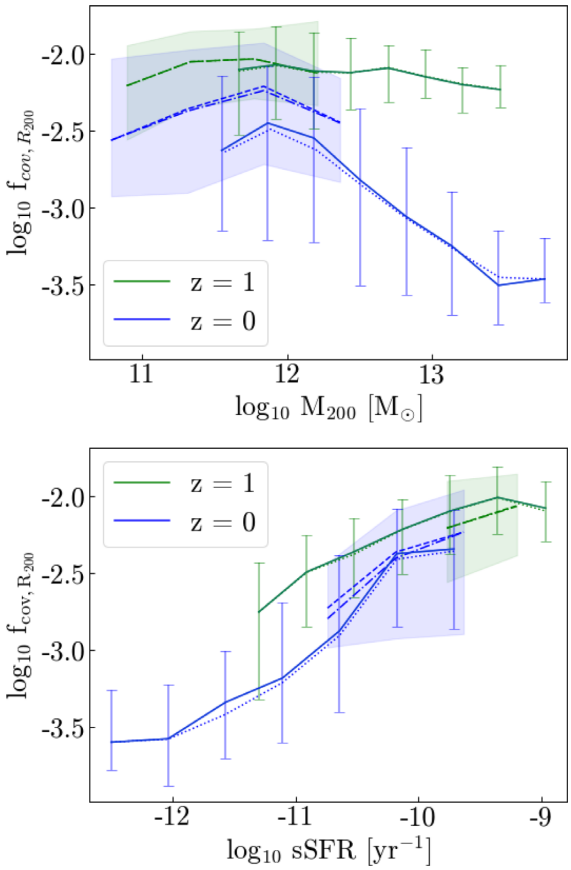


Figure A2. Plots of $f_{\mathrm{cov},R_{200}}$ versus M_{200} (left) and sSFR (right). In each plot, the results from $z = 1$ are shown in green and those from $z = 0$ are in blue. The solid/dashed lines indicate the median values of $f_{\mathrm{cov},R_{200}}$ in halo mass/sSFR bins calculated using the K13 H I–H_2 breakdown method in the RefL0100/RecalL0025 EAGLE boxes. Alternatively, the dotted/dot–dashed lines indicate the median values calculated using the G11 model for the RefL0100/RecalL0025 simulations. The vertical lines and shaded regions indicate the 16th–84th percentile ranges calculated for the G11 results in the RefL0100 and RecalL0025 simulations, respectively.

$$\alpha = \frac{5G_0'/2}{1 + (G_0'/2)^2}, \tag{A6}$$

and

$$D_\star = 1.5 \times 10^{-3} \times \ln(1 + (3G_0')^{1.7}), \tag{A7}$$

respectively. Here, we have substituted our value of the UV field for G_0', calculated using different methods for the SF and NSF particles, as detailed in Section 2.3.1.

Fig. A1 shows there is minimal impact on the overall $M_{\mathrm{H\,I}}$–$M_\star$ relation by using the Gnedin & Kravtsov (2011) H I–H_2 breakdown method described above (from now on described as G11) instead of the theoretically motivated Krumholz (2013) method (K13) described in Section 2.3.1. This is true for both the RecalL0025 and RefL0100, and is also seen at low and high redshift. These results show that changing the H I model has minimal impact on the global H I properties of resolved galaxies in the simulations.

We next explore the impact of changing the H I–H_2 breakdown method on the redshift evolution of the $f_{\mathrm{cov,R_{200}}}$–M_{200} relation (Fig. A2). We can see the trends that were central to our results in the paper – namely the change in gradient seen between $z = 0$ and

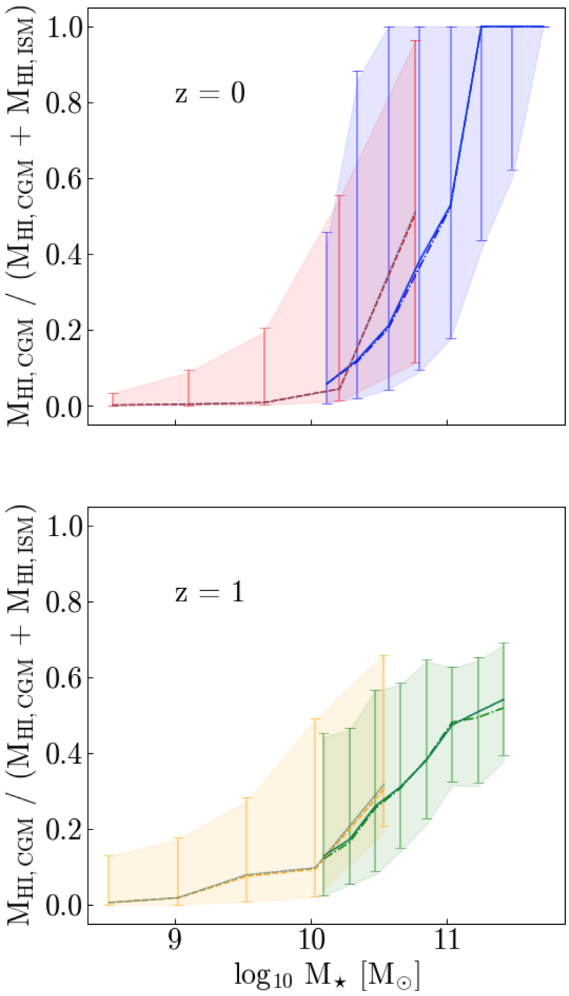


Figure A3. Plots of the mass of H I in CGM as a fraction of the total H I mass in the ISM and CGM, as a function $M_\star$ at $z = 0$ (left) and $z = 1$ (right). The median values across bins in stellar mass are shown as solid (dashed) lines for the results calculated using the K13 (G11) H I–H_2 breakdown method. The shaded regions indicate the 16th–84th percentile ranges for the G11 results, while the vertical lines indicate the same for the K13 results. The results from the RecalL0025 galaxy sample are shown in red/orange (redshift 0/1), while those taken from RefL0100 are shown in blue/green.

$z = 1$ along with the peak at $\sim 10^{12}$ $M_\odot$ at $z = 0$ – are still present when using the G11 method, indicating the convergence in total H I mass/global H I properties seen in Fig. A1 extends to the highest column density H I in each galaxy.

Finally, we investigate the impact of the H I–H_2 method on the relative mass of H I in the CGM compared with the ISM in Fig. A3. Here, we plot the mass of H I in the CGM as a fraction of the total H I mass in both the CGM and ISM, as a function of stellar mass. Comparing the results from G11 to those found using the K13 method, we see they are more or less identical – the G11 results show the same reduction in the slope of this relation with redshift, along with a global increase in the CGM H I mass fraction seen in galaxies with stellar mass $<10^{10}$ $M_\odot$ with increasing redshift. This agreement in the CGM/ISM H I breakdown between different methods gives validity to our conclusions that a significant fraction of H I lies in the CGM in high-mass galaxies across the range of redshift studied here.

Downloaded from https://academic.oup.com/mnras/article/501/3/4396/6041704 by Bodleian Library of the University of Oxford user on 01 April 2021

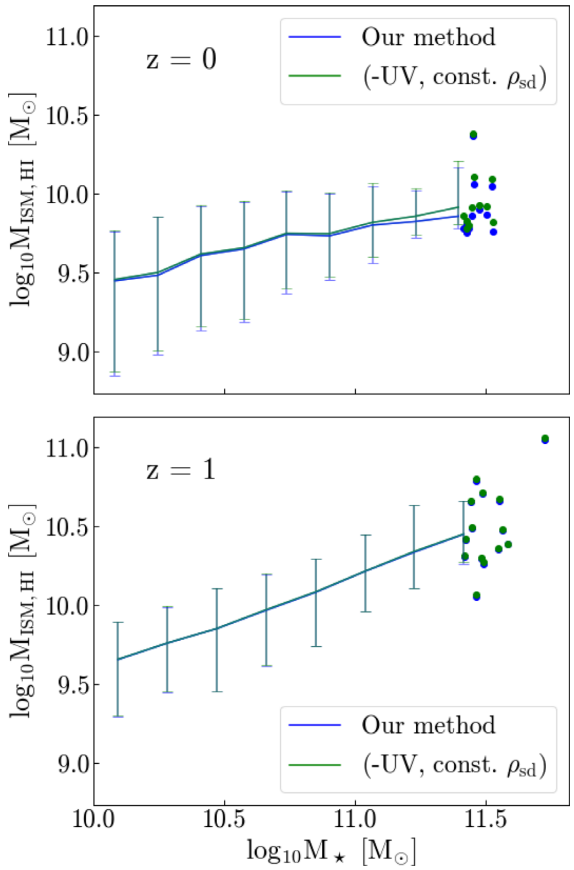


Figure A4. Plots of the median mass of H I in ISM using bins in $M_\star$ at $z = 0$ (top panel) and $z = 1$ (lower panel) using galaxies taken from RefL0100, as calculated using two different H I–H_2 breakdown methods; the first is our fiducial method in blue, described in Section 2.3.1, while the second (in green) does not include the UV propagation from SF particles and uses a constant value for the total matter density (ρ_{sd}, as referenced in equation 7). The 16th–84th percentile ranges are shown using the vertical, capped lines.

A2 Other alterations to the H I–H_2 breakdown method

We also explored the effect of including the additional UV propagation mechanism (detailed in Section 2.3.1) and a non-constant background matter density (ρ_{sd}, referenced in equation 7), again finding our results do not change significantly, in particular the H I masses do not vary significantly, along with the DLA covering fractions. The largest difference in the H I masses occurs in particles we ascribe to the ISM (see Section 2.4 for our detailed ISM/CGM breakdown); the CGM masses do not vary between the two H I–H_2 breakdown methods. This is demonstrated in Fig. A4; the ISM H I mass is reduced in high-stellar-mass galaxies ($>10^{11}$ $M_\odot$) at $z = 0$. On further investigation, we found the lost H I mass is instead considered to be H_2 in our fiducial method (which includes UV propagation). This is primarily because the Wolfire et al. (2003) two-phase model dominates in both the ISM and CGM (see Fig. 19); and in this regime the CNM number density is set by the minimum pressure required to maintain the CNM alongside the WNM, which in turn is directly proportional to the UV flux (see equation 6). Since the additional UV flux from the propagation of UV to NSF particles is greater in the ISM compared with the CGM, the associated increase in the density of the CNM is also greater, along with the assumed optical depth of the dust (see equation 13), leading to a larger H_2 mass fraction and subsequently a smaller H I mass fraction.

This paper has been typeset from a TEX/LATEX file prepared by the author.

Downloaded from https://academic.oup.com/mnras/article/501/3/4396/6041704 by Bodleian Library of the University of Oxford user on 01 April 2021